LRRC23 truncation impairs radial spoke 3 head assembly and sperm motility underlying male infertility

Jae Yeon Hwang[1,2,†], Pengxin Chai[3,†], Shoaib Nawaz[4,11,†], Jungmin Choi[5,6], Francesc Lopez-Giraldez[7], Shabir Hussain[8,12], Kaya Bilguvar[5,7], Shrikant Mane7[6], Richard P. Lifton[9], Wasim Ahmad[4,8], Kai Zhang[3], Jean-Ju Chung[1,10,*]

[1]Department of Cellular and Molecular Physiology, Yale School of Medicine, Yale University, New Haven, CT, 06510; [2]Present address, Department of Molecular Biology, Pusan National University, Pusan, South Korea, 43241; [3]Department of Molecular Biophysics and Biochemistry, Yale School of Medicine, Yale University, New Haven, CT, 06510; [4]Department of Biotechnology, Faculty of Biological Sciences, Quaid-i-Azam University, 45320, Islamabad, Pakistan; [5]Department of Genetics, Yale School of Medicine, Yale University, New Haven, CT, 06510; [6]Department of Biomedical Sciences, Korea University College of Medicine, Seoul, South Korea, 02841; [7]Yale Center for Genome Analysis, Yale University, West Haven, CT, 06516; [8]Department of Biochemistry, Faculty of Biological Sciences, Quaid-i-Azam University, 45320, Islamabad, Pakistan; [9]Laboratory of Human Genetics and Genomics, The Rockefeller University, New York, NY, 10065; [10]Department of Obstetrics, Gynecology and Reproductive Sciences, Yale School of Medicine, Yale University, New Haven, CT, 06510; [11]Present address, Department of Human Genetics, Sidra Medicine, Doha, Qatar, 26999; [12]Present address, Clinical and Molecular Metabolism Program, Faculty of Medicine, University of Helsinki, Helsinki, Finland, 00250

[†]These authors contributed equally to this work.

*Correspondence to Jean-Ju Chung: jean-ju.chung@yale.edu

Keywords: Male infertility, WES, Sperm flagella, Radial spoke, Cryo-ET

Abstract

Radial spokes (RS) are T-shaped multiprotein complexes on the axonemal microtubules. Repeated RS1, RS2, and RS3 couple the central pair to modulate ciliary and flagellar motility. Despite the cell type specificity of RS3 substructures, their molecular components remain largely unknown. Here, we report that a leucine-rich repeat-containing protein, LRRC23, is an RS3 head component essential for its head assembly and flagellar motility in mammalian spermatozoa. From infertile male patients with defective sperm motility, we identified a splice site variant of *LRRC23*. A mutant mouse model mimicking this variant produces a truncated LRRC23 at the C-terminus that fails to localize to the sperm tail, causing male infertility due to defective sperm motility. LRRC23 was previously proposed to be an ortholog of the RS stalk protein RSP15. However, we found that purified recombinant LRRC23 interacts with an RS head protein RSPH9, which is abolished by the C-terminal truncation. Evolutionary and structural comparison also shows that LRRC34, not LRRC23, is the RSP15 ortholog. Cryo-electron tomography clearly revealed that the absence of the RS3 head and the sperm-specific RS2-RS3 bridge structure in LRRC23 mutant spermatozoa. Our study provides new insights into the structure and function of RS3 in mammalian spermatozoa and the molecular pathogenicity of LRRC23 underlying reduced sperm motility in infertile human males.

Introduction

Motile cilia and flagella are evolutionarily conserved organelles essential for cellular motility (Inaba, 2011; Ishikawa, 2017). The core of motile cilia and flagella is the '9+2' axoneme, characterized by a scaffold structure composed of nine peripheral microtubule doublets (MTDs) and a central pair of singlet microtubules (CP). Each MTD binds two rows of dyneins, the outer-arm dyneins (OAD) and inner-arm dyneins (IAD), which generate mechanical force required for the ciliary beating via ATP hydrolysis (Kubo *et al*, 2021; Rao *et al*, 2021). Radial spoke (RS) controls the amplitude of the ciliary and flagellar beat by transmitting mechanochemical signals from the CP to the axonemal dyneins (Smith & Yang, 2004; Viswanadha *et al*, 2017). In *Chlamydomonas reinhardtii*, RS mutations paralyze the flagellar movement (Witman *et al*, 1978) and the axoneme lacking RS system shows reduced velocity of microtubule sliding by dyneins (Smith & Sale, 1992). In human and mouse, mutations in RS components or their absence cause primary ciliary dyskinesia (PCD) and/or male infertility due to the defective ciliary and flagellar beating (Abbasi *et al*, 2018; Liu *et al*, 2021; Sironen *et al*, 2020). These studies highlight the physiological importance of RS in regulating ciliary and flagellar movement.

A triplet of three RSs (RS1, RS2, and RS3) repeats every 96-nm along the peripheral MTDs and this 96-nm periodicity of RS is well-conserved in cilia and flagella across diverse organisms (Viswanadha *et al.*, 2017; Zhu *et al*, 2017). RS is a multiprotein complex; at least 23 RS components were identified in *C. reinhardtii* (Gui *et al*, 2021; Viswanadha *et al.*, 2017; Yang *et al*, 2006). These RS components are also crucial for RS organization and function in other ciliated and flagellated organisms (Bazan *et al*, 2021; Ralston *et al*, 2006; Sironen *et al.*, 2020; Urbanska *et al*, 2015), indicating evolutionarily conserved molecular composition of the RS. However, cryo-electron microscopy (cryo-EM) studies have revealed species- and tissue-specific structural variabilities in RS3. For example, RS3 in most species is a T-shaped axonemal structure that consists of a head and a stalk like those of RS1 and RS2 (Imhof *et al*, 2019; Leung *et al*, 2021; Lin *et al*, 2014; Pigino *et al*, 2011) but RS3 in *C. reinhardtii* is a headless and stump-like structure (Pigino *et al.*, 2011). In addition, mammalian sperm flagellar axoneme carries a unique bridge structure between RS2 and RS3 (Leung *et al.*, 2021), which is not observed from tracheal cilia as well as other flagellated organisms (Imhof *et al.*, 2019; Lin *et al.*, 2014). This variability suggests that RS3 is an evolutionarily more divergent structure and conveys species- and/or tissue-specific ciliary and flagellar function. Yet, the overall molecular composition of RS3 and the extent to which RS3 components are species- and/or tissue specific remains largely unknown.

Asthenozoospermia (ASZ) is the male infertility classified by reduced sperm motility (World Health Organization, 2010). ~80% of male infertile patients manifest sperm motility defects (Curi *et al*, 2003) as infertile male with abnormal sperm morphology and/or reduced sperm count often accompany low motility (Cavarocchi *et al*, 2022; Toure *et al*, 2021). Recent whole exome sequencing studies identified genetic defects in RS components from idiopathic ASZ patients (Liu *et al.*, 2021; Martinez *et al*, 2020; Shen *et al*, 2021). Mutant analyses using model organisms further elucidated the function of RS components in the flagellar movement and the pathogenic mechanisms (Liu *et al.*, 2021; Martinez *et al.*, 2020). Thus, WES combined with functional and structural analyses of mutants, especially in a mouse model, would be a powerful and direct approach to understand mammalian specific RS3 roles including sperm motility regulation and genetic etiologies causing male infertility.

Here, we report a bi-allelic loss-of-function splicing variant in *LRRC23* from ASZ patients in a Pakistani consanguineous family. We generated a mouse model that mimics the human mutation and found that the mutation leads to C-terminal truncated LRRC23 and that the mutant mice

phenocopy the impaired sperm motility and male infertility. Using biochemical analyses and structural prediction, we showed that, different from previously known, LRRC23 is not the ortholog of a RS2 stalk protein RSP15 but interacts with a known RS head protein. Finally, we visualized the in-cell structures of RS triplets in intact WT and mutant sperm using cryo-electron tomography (cryo-ET). We observed missing RS3 head and aberrant junction between RS2 and RS3 in the mutant flagellar axoneme, unarguably demonstrating that LRRC23 is a head component of RS3. This study provides molecular pathogenicity of *LRRC23* in RS-associated ASZ and reveals unprecedented structural insights into the RS3 and its implication in normal sperm motility and male fertility in mammals.

Results

A Loss of Function Splice Site Variant Truncating LRRC23 is Identified from a Consanguineous Family with Asthenozoospermia

A consanguineous Pakistani family with infertile males was recruited (Fig 1 A). Both infertile males (IV-1 and IV-2) have failed to have child over 3 years of unprotected sex after marriage (Table EV1). The male infertile patients do not show PCD-related symptoms, abnormal heights, weights, secondary characteristics, nor anatomical defects. They also have normal karyotypes without Y chromosome microdeletion. Overall, the Papanicolaou (PAP) stained spermatozoa from the infertile patients showed an overall normal morphology (Figs 1B and EV1A), which was further supported by normal ranges of abnormal sperm morphology assessed by clinical semen analysis (Table EV1). However, their progressive motility was lower than the World Health Organization (WHO) standard (World Health Organization, 2010) and the patients were clinically diagnosed as ASZ (Table EV1). To understand the genetic etiology underlying the defective sperm motility, we performed whole exome sequencing (WES) on the proband, IV-1. WES estimated 5.02% inbreeding co-efficiency and the longest homozygous-by-descent segment as 37.5 cM, verifying the consanguineous nature of the recruited family. Among the four identified rare variants (Table EV2), only one homozygous splicing donor site variant (c.621+1G>A) in *LRRC23* (leucin-rich repeat containing protein 23) is co-segregated with the male infertility phenotype (Fig 1A, C, and D). Of note, a female sibling (IV-4) who also has the homozygous *LRRC23* variant (IV-4) is infertile because her partner was able to have children from his second marriage (Fig 1A). However, the infertility of IV-4 is not likely be due to the variant because the mother (III-1) also carries the homozygous allele but was fertile (Fig 1A). The variant at the splicing donor site of *LRRC23* intron 5 is predicted to prevent splicing out of the intron, which can lead to early termination of protein translation with loss of 136 amino acids at the C-terminus (Fig EV1B and C). To verify the splicing defects and generation of mutant protein by the variant, we constructed minigenes to express *LRRC23* ORF spanning partial intron 5 with the normal or variant sequence at the splicing site in 293T cells (Fig 1E). 293T cells transfected with the construct carrying the variant failed to splice out the intronic region (Fig 1F) and generated only truncated LRRC23 (Fig EV1D). These results suggest the variant is pathogenic and explains the male infertility with defective sperm motility in this family.

C-terminally Truncated LRRC23 Fails to Localize in the Flagella and Causes Defective Sperm Motility

LRRC23 is a radial spoke (RS) component (Padma *et al*, 2003). Consistent with the ASZ phenotype in our infertile patients with a new splice mutation in *LRRC23*, genetic ablation of *Lrrc23* in mice causes severe sperm motility defects and male infertility (Zhang *et al*, 2021). However, how the C-terminus truncation of LRRC23 affects the RS structure and function remains unresolved. To better understand detailed function of LRRC23 and the molecular pathogenicity of the identified variant, we generated *Lrrc23* mutant mice by CRISPR/Cas9 genome editing to mimic the predicted outcome in human patients (Figs EV1 and EV2A). We targeted two regions, one in intron 5 and the other in intron 7 (Fig EV2B) to delete exon 6 and 7 together and express truncated LRRC23 at C-terminus. We established two mouse lines with 4,126 or 4,135 bp deletion (*Lrrc23-4126del* and *Lrrc23-4135del*, respectively) (Fig EV2C). Both homozygous *Lrrc23-4126del* and *4135del* mice displayed the identical male infertility and defective sperm motility phenotypes in our initial characterization. In this study, we used *Lrrc23-4126del* line as *Lrrc23-mutant* line unless indicated. We observed that truncated *Lrrc23* mRNA is expressed from the mutant *Lrrc23* allele but the total mRNA level of *Lrrc23* in testis is not different from wildtype (WT) to that in *Lrrc23*$^{\Delta/\Delta}$ males (Fig EV2D-F). Sequencing the truncated *Lrrc23* mRNA revealed that the transcript would produce mutant LRRC23 containing 27 non-native

amino acids translated from 3' UTR instead of 136 amino acids at the C-terminus (Fig EV2G). Despite the comparable *Lrrc23* mRNA levels in WT and *Lrrc23*$^{\Delta/\Delta}$ testis, the truncated LRRC23 is detected only marginally in the microsome fraction of *Lrrc23*$^{\Delta/\Delta}$ testis, different from full-length LRRC23 enriched in the cytosolic fraction of WT testis (Figs 2A and EV3A and B). In addition, the mutant LRRC23 is not present in epididymal sperm (Figs 2B and C, and EV3C-E)**,** indicating that the C-terminal region is essential for proper LRRC23 transportation to the sperm flagella.

Sperm from *Lrrc23*$^{\Delta/\Delta}$ and *Lrrc23-4135del*$^{\Delta/\Delta}$ males are morphologically normal (Figs 2C and EV3E and F) and the epididymal sperm counts of *Lrrc23*$^{+/\Delta}$ and *Lrrc23*$^{\Delta/\Delta}$ males are not significantly different (Fig 2D). Despite the normal morphology and sperm counts, *Lrrc23*$^{\Delta/\Delta}$ males are 100% infertile (Fig 2E and F). By contrast, *Lrrc23*$^{\Delta/\Delta}$ females are fertile, which supports the IV-4's infertility is not likely due to the identified variant (Fig 1A). To further understand how the homozygous *Lrrc23* mutation causes male infertility, we performed Computer Assisted Semen Analysis (CASA). *Lrrc23*$^{\Delta/\Delta}$ sperm motility parameters are significantly altered compared to *Lrrc23*$^{+/\Delta}$ sperm (Fig EV3G). *Lrrc23*$^{\Delta/\Delta}$ sperm cannot swim efficiently under viscous conditions that mimic the environment in female reproductive tract (Fig 2G; Movie EV1), and their flagella just vibrate but do not beat normally (Figs 2H and EV3H; Movie EV2). In addition, inducing capacitation did not rescue any observed motility defect of *Lrrc23*$^{\Delta/\Delta}$ sperm as demonstrated by flagellar waveform analysis, and CASA measurement of curvilinear velocity (VCL), straight line velocity (VSL), and amplitude of lateral head (ALH). These results suggest the C-terminal truncation dysregulates the flagellar localization of the mutant LRRC23, leading to sperm motility defects and male infertility.

C-terminal Truncation of LRRC23 Abolishes its Interaction with Radial Spoke Head

Recent cryo-ET studies revealed that T-shaped RS structures (i.e., head and stalk) are conserved across the species (Leung *et al.*, 2021; Lin *et al.*, 2014) (Fig. 3 A). Three RSs (RS1, RS2, and RS3) are repeated in a 96-nm interval along the flagellar axoneme in mammalian sperm, sea urchin sperm, *Trypanosoma brucei*, and even in *C. reinhardtii* with stump-like RS3 without a head structure (Fig. 3 A). LRRC23 is a RS protein in chordate axoneme and has been considered especially as the orthologue of RSP15, a RS2 stalk protein in *C. reinhardtii* (Han *et al*, 2018; Satouh & Inaba, 2009; Yang *et al.*, 2006; Zhang *et al.*, 2021) (Fig 3B). We initially hypothesized the C-terminal truncation of LRRC23 affects the assembly of a RS stalk and/or its incorporation into the RS2. Thus, we tested the protein-protein interaction of normal (hLRRC23^{WT}) and mutant (hLRRC23^{Mut}) human LRRC23 with known RS stalk (RSPH3, RSPH22) or head (RSHP6A, RSHP9) proteins using RSPH-trap assay (Figs 3C-E and EV4A). Purified GST-tagged hLRRC23^{WT} and hLRRC23^{Mut} proteins (Fig 3C and D) were incubated with a recombinant human RSPH enriched by immunoprecipitation (Fig 3E). This trap assay demonstrated that hLRRC23^{WT} interacts only with RSPH9, a RS head protein, among the head and stalk RSPH proteins tested (Figs 3F and EV4B). Interestingly, the previously reported interaction between LRRC23 and RSPH3 (Zhang *et al.*, 2021) is not detected in our assay, which may be due to the different interaction conditions used *in vitro*. Markedly, hLRRC23^{Mut} does not interact with RSPH9, indicating LRRC23 interaction with RS head via its C-terminus. This result also raises the question whether LRRC23 is a head protein of RS, not a stalk protein, a different picture from previous studies. To test this new hypothesis, we performed BLAST search and found *C. reinhardtii* RSP15 (Gui *et al.*, 2021) has the highest sequence homology to LRRC34, not LRRC23, in *Ciona intestinalis*. Our phylogenetic and pairwise distance comparison analyses also revealed that LRRC34 orthologs are evolutionarily closer to RSP15 orthologs than LRRC23 orthologs (Figs 3G and EV4C). Moreover, AlphaFold-predicted structure of human LRRC34, but not that of LRRC23, presents the same structural features as those of RSP15 (i.e., repeated leucin-rich repeat domains and an α-helix motif in-between) (Fig 3H). *LRRC34* and *LRRC23* share their

gene expression patterns among tissues, most abundantly expressed in the tissues known for ciliary and flagellar function such as retina, testis, and fallopian tube (Fig EV4D and E). All these results suggest that LRRC34 is a ciliary and flagellar protein and likely the RSP15 orthologue in chordates, and that LRRC23 function is associated with the RS head.

LRRC23 Mutation Disorganizes Radial Spoke 3 in Sperm Flagella

Next, we examined the impact of LRRC23 loss of function by the C-terminal truncation on the subcellular and ultrastructural organization of sperm. We first compared flagellar compartmentalization between *Lrrc23*$^{+/\Delta}$ and *Lrrc23*$^{\Delta/\Delta}$ sperm. Confocal imaging of immunostained sperm by antibodies against various proteins of known localization did not show any difference on the subflagellar localization of axonemal or peri-axonemal proteins (Fig 4A and EV5A). The levels of such flagellar proteins are also not significantly different between *Lrrc23*$^{+/\Delta}$ and in *Lrrc23*$^{\Delta/\Delta}$ sperm (Fig EV5B and C). Furthermore, transmission electron microscopy (TEM) did not reveal apparent structural abnormalities in *Lrrc23*$^{\Delta/\Delta}$ sperm flagella (Figs 4B and EV5D). These results indicate overall subflagellar and ultrastructural organization in *Lrrc23*$^{\Delta/\Delta}$ sperm is preserved despite almost complete loss of sperm motility. Any structural abnormality in *Lrrc23*$^{\Delta/\Delta}$ sperm would be subtle and local in the axoneme, likely in the RS head region, which requires a higher resolution microscope technique.

To determine how the absence of LRRC23 affects sperm structure in more detail, we performed cryo-ET 3D reconstruction to visualize substructural changes of the sperm axoneme (Fig 4C and Movie EV3). The reconstructed tomogram slices revealed striking details of the RS structural difference between WT sperm and *Lrrc23*$^{\Delta/\Delta}$ sperm (Fig 4C). In WT sperm, the three RSs are repeated with a typical pattern, in which RS1 and RS2 are recognized by an additional EM density between them (barrel structure, Leung *et al.*, 2021) followed by RS3 (Fig 4C, *left*). In *Lrrc23*$^{\Delta/\Delta}$ sperm, EM densities corresponding to RS3 are significantly weaker than those in WT sperm whereas the structural features of RS1 and RS2 are overall kept unaltered from that of WT sperm (Fig 4C*, right*). These results strongly indicate that the LRRC23 mutation specifically disorganizes RS3 in the sperm axoneme.

LRRC23 Is a Head Component of Radial Spoke 3

To visualize the structural defects of RS3 along the *Lrrc23*$^{\Delta/\Delta}$ sperm axoneme in more detail (Fig 4C), we performed sub-tomogram averaging (STA) of the axonemal doublets in 96 nm repeat (i.e., the distance that spans a single set of RS1, RS2, and RS3) on both WT and *Lrrc23*$^{\Delta/\Delta}$ spermatozoa (Figs 5 and EV6). Remarkably, the resulting 3D maps reveal that the head region of RS3 is entirely missing in *Lrrc23*$^{\Delta/\Delta}$ sperm whereas the heads of RS1 and RS2 are intact (Fig 5A and B). In addition, superimposition of the 3D STA maps demonstrates that the junctional structure between RS2 and RS3–present in mouse and human sperm but not in *C. reinhardtii* nor in *T. brucei* flagellar axoneme–is also specifically abolished in *Lrrc23*$^{\Delta/\Delta}$ sperm (Fig 5C). By contrast, *Lrrc23*$^{\Delta/\Delta}$ sperm have intact stalk structures of RS3 like those in WT sperm. Consistent with the protein-protein interaction between LRRC23 and the RS head protein RSPH9 using the RSPH-trap approach (Fig 3), these direct structural observations unarguably clarify that LRRC23 is a RS3 head component and the absence of the RS3 head leads to motility defects in *Lrrc23*$^{\Delta/\Delta}$ sperm. These results demonstrate that the C-terminal truncation of LRRC23 prevents the assembly of RS3 head during spermatogenesis, thus preventing functional RS3 complex formation. Taken together, our functional and structural studies using the mouse model recapitulating the human mutation elucidate the molecular pathogenicity of LRRC23 underlying impaired sperm motility and male infertility (Fig 5D).

Discussion

LRRC23 is a Distinct Head Component of Radial Spoke 3

Accumulating evidence on the structural heterogeneity of radial spokes in cilia and flagella suggests that the molecular organization and function of RS3 is distinct from those of RS1 and RS2. For example, the morphology of RS3 head is distinguished from those of RS1 and 2 in mouse motile cilia (Zheng *et al*, 2021). Moreover, in the tracheal cilia of the PCD patients, RSPH1 or RSPH4 loss-of-function mutation specifically abolished RS1 and RS2 heads, but not RS3 head (Lin *et al.*, 2014; Zhao *et al*, 2021) even though RS3 shares T-shaped structure just like RS1 and RS2 in most eukaryotic motile cilia and flagella (Imhof *et al.*, 2019; Leung *et al.*, 2021; Lin *et al*, 2012; Lin *et al.*, 2014). Despite these findings, the molecular composition of RS3 head remains largely unknown. The current study demonstrates that LRRC23 is a RS3-specific head component. Previous immuno-EM studies showed that LRRC23 is a conserved RS protein in *C. intestinalis* and mouse (Pigino *et al.*, 2011; Zhang *et al.*, 2021). It is of note that LRRC23 was originally predicted to be the orthologue of RSP15 in *C. reinharditti*, a RS2 stalk protein, due to the presence of leucine-rich repeat domains (Gui *et al.*, 2021; Yang *et al.*, 2006). Yet, we found LRRC23 orthologues are not conserved in *C. reinharditti* in which RS3 is headless and short stump-like, but present in the species where RS3 head structure is preserved, such as *T. thermophila*, sea urchin, and mammals. Instead of LRRC23, our phylogenetic and structural comparison strongly suggests that LRRC34 is likely the RSP15 orthologue in chordate animals (Figs 3 and EV4) and a previously unappreciated component of RS2 stalk. Identifying a LRRC34 loss-of-function mutation from ciliopathic children further supports that LRRC34 is a RS component (Shamseldin *et al*, 2020). Our wild type-mutant comparison approach using cryo-ET analyses ultimately clarify that LRRC23 is required for assembling the RS3 head structure (Figs 4 and 5), indicating LRRC23 as a RS3 head component. Interestingly, a RS head component, RSPH9, interacts with LRRC23 but the protein level or the localization of RSPH9 is not altered in *Lrrc23*$^{\Delta/\Delta}$ sperm (Fig EV4), suggesting that RSPH9 could be a head component of RS1 and RS2 like in *C. reinhardtii* (Gui *et al.*, 2021), but not of RS3. Of note is that an independent study reported that LRRC23 is required for flagellar localization of the RS stalk and fibrous sheath components in mature sperm (Zhang *et al.*, 2021). This discrepancy between two studies is likely due to the presence of the truncated LRRC23 in testis in *Lrrc23*$^{\Delta/\Delta}$ males, which might partly allow flagellar localization of other flagellar components during germ cell development. Although the full picture of molecular composition of RS3 head remains to be revealed, our findings demonstrate LRRC23 is a RS3-specific head component. This conclusion is further supported by the presence of LRRC23 in tracheal cilia (Zhang *et al.*, 2021) that lack the RS2-RS3 bridge structure (Leung *et al.*, 2021).

LRRC23 is required for mammalian sperm-specific bridge structure between RS2 and RS3

In motile cilia and flagella, a set of three RSs is repeated along the axoneme (Leung *et al.*, 2021; Lin *et al.*, 2012; Lin *et al.*, 2014; Viswanadha *et al.*, 2017). Notably, a recent cryo-ET study revealed additional RS substructures in mammalian sperm flagella, a barrel structure at RS1 and a junctional bridge structure between RS2 and RS3 (Leung *et al.*, 2021), which were not observed in the sea urchin sperm or human motile cilia (Lin *et al.*, 2014). Furthermore, they are asymmetrically distributed along the mammalian sperm axoneme, corresponding to the peripheral MTDs in a species-specific manner (Chen *et al*, 2023). Our cryo-ET and STA analyses visualized the mammalian sperm-specific RS1 barrel and RS2-RS3 bridge structures in WT sperm flagella, consistent with Leung et al (Leung *et al.*, 2021). Strikingly, in *Lrrc23* mutant sperm, most of the EM density corresponding to the RS2-RS3 bridge structure is missing and/or altered together with that of the RS3 head (Figs 4 and 5). Considering the absence of RS2-RS3 bridge in tracheal cilia (Lin *et al.*, 2014), LRRC23 also contributes to assemble this flagellar RS substructure. Thus, we speculate that the RS3 and RS2-RS3 bridge structures and their sub-axonemal localization confer non-planar and asymmetric flagellar motility unique to mammalian sperm hyperactivation. As the RS2-RS3 bridge structure is absent in tracheal cilia (Lin *et al.*, 2014), our study unambiguously demonstrates that LRRC23 is required for assembling this bridge structure

specifically in mammalian sperm flagella. If so, LRRC23 may be localized at the junction between RS2-RS3 bridge structure and RS3 head. The detailed molecular components that comprise the RS2-RS3 bridge require further study. Profiling and comparing LRRC23 interactomes from mammalian motile cilia and sperm flagella could unveil the cell-type specific molecular organization of RS3.

LRRC23 loss of function causes male infertility in mice and human

Loss-of-function mutations in various RS components that are common to motile cilia and sperm flagella were reported to cause PCD and/or male infertility. Loss-of-function mutations of RSPH1 (Knowles *et al*, 2014; Kott *et al*, 2013), RSPH3 (Jeanson *et al*, 2015), RSPH4A and RSPH9 (Castleman *et al*, 2009) were identified from PCD patients. Some of the male patients carrying RSPH1 and RSPH3 mutations were infertile (Jeanson *et al.*, 2015; Knowles *et al.*, 2014). RSPH1, RSPH4A, and RSPH9 knockout mouse models recapitulated the PCD phenotypes such as hydrocephalus and impaired mucociliary clearance (Yin *et al*, 2019; Yoke *et al*, 2020; Zou *et al*, 2020). However, there are other RS components in which mutations only cause male infertility in mice and human. For example, WES of infertile males without PCD symptoms identified mutations in CFAP251 (Auguste *et al*, 2018; Kherraf *et al*, 2018) and CFAP61 (Liu *et al.*, 2021; Ma *et al*, 2021). RSPH6 (Abbasi *et al.*, 2018), CFAP251 (Kherraf *et al.*, 2018), or CFAP61 (Liu *et al.*, 2021) deficiency also rendered male mice infertile but without gross abnormalities. These phenotypic differences could be due to a different physiological role of the individual RS component between motile cilia and flagella or a distinct repertoire of the RS components that permits functional redundancy. In our study, LRRC23 mutant mice do not have any apparent gross abnormality but display male infertility (Fig 2). Considering the altered interaction of truncated LRRC23 with RSPH9 *in vitro* (Fig 2), the LRRC23 interaction with RSPH9 is presumably essential for the RS organization and/or sperm motility in mammals. However, since we only examined the interaction of the human proteins, there may be species-specific differences that need to be further investigated. Consistent with our study, a previous study found immotile sperm but normal tracheal ciliary beating in the absence of LRRC23 (Zhang *et al.*, 2021). Supportive of these observations, the infertile male patients in the current study do not show PCD symptoms. This phenotype of male infertility without PCD symptoms in both mice and human suggests the mammalian sperm-specific role of LRRC23 in RS structure and function. Physiological implication of LRRC23 and RS3 in motile cilia is unclear but it is likely dispensable for normal ciliary movement probably due to compensatory and/or redundant RS3 proteins specific to cilia. Whether LRRC23 absence would lead to similar structural aberration in RS3 head of motile cilia requires further study. Intriguingly, LRRC23 loss-of-function impairs primarily flagellar motility but morphology only marginally, which is in distinct from other RS components. For example, the absence of RSPH6, CFAP251, or CFAP61 causes male infertility without PCD symptoms but displays multiple morphological abnormalities of the flagella characterized by absent, short, bent, coiled, and irregular flagella (Toure *et al.*, 2021). By contrast, LRRC23 mutation and absence do not cause either PCD nor MMAF phenotypes in human and mouse, suggesting a distinct physiological significance of LRRC23 in reduced sperm motility.

Materials and Methods

Subject and family

This study was approved from the review board of Quaid-i-Azam University, Islamabad, Pakistan (IRB00003532, IRB protocol # QAU-171) and the Yale Center for Mendelian Genomics. The family members recruited in this study were explained about the procedure and possible outcomes. The family members provided written consent to attend this study.

Sample collection and clinical investigation

Semen Semen samples were collected and clinically analyzed according to WHO guidelines (World Health Organization, 2010). Semen samples were collected from the infertile male members after 2-5 days of abstinence from sexual intercourse. The collected semen samples were subjected to the clinical analysis by expert laboratory technologists at Aga Khan Medical Centre (Gilgit, Pakistan) to measure pH, volume, viscosity, and color of the semen and sperm parameters. To assess sperm motility and morphology, the collected semen was liquefied at 37 °C for 30-60 minutes. A minimum of 1,000 spermatozoa were counted to analyze sperm motility by the CASA system using an MTG-GmbH analyzer (version 5.4; MTG-MedeaLAB) according to the unit's standard operating procedures based on the WHO guidelines as previously reported (Krause *et al*, 2016; Nawaz *et al*, 2021; Slabbert *et al*, 2015). Sperm from liquified semen were subjected to PAP-staining and the morphology was microscopically analyzed according to the guidelines from WHO and evaluated by a reproductive medicine specialist. PAP-stained sperm were imaged using CMOS camera (Basler acA1300-200µm, Basler AG) equipped in Nikon E200 microscope.

Blood Venous blood samples were collected from attending family members. Collected blood samples were used for karyotyping and genomic DNA extraction. Blood cells cultured with phytohemagglutinin for 72 hours were used for karyotyping. The cultured cells were disrupted and Giemsa-stained. Twenty metaphases were examined to examine karyotypes of each member. Genomic DNA (gDNA) samples were extracted using QIAamp DNA Kit (QIAGEN, Germany). Extracted gDNA samples were subjected to examine microdeletions at the Y-chromosome (AZFa, AZFb, AZFc, and AZFd), whole exome sequencing (WES), and Sanger Sequencing.

Whole-Exome Sequencing and Data Analysis

Whole exome sequencing was carried out as described in our previous study (Hwang *et al*, 2021b). Briefly, 1.0 µg of genomic DNA from proband's blood is fragmented to an average length of 140 bp using focused acoustic energy (Covaris E210). DNA fragments were subjected to exome capturing using the IDF xGen capture probe panel with an additional "spike-in" of ~2,500 region which are total 620 kb of RefGene coding regions. The captured fragments were pair-end sequenced by 101 bp reading using NovaSeq 6000 with S4 flow cell (Illumina). Sequenced reads were aligned to reference human genome (GRCh37/hg19) using the BWA-MEM (Li, 2013) and processed to generate variants using GATK v3.4 (McKenna *et al*, 2010; Van der Auwera *et al*, 2013). Variants were annotated with ANNOVAR (Wang et al., 2010) and the predicted deleteriousness of non-synonymous variants was determined by MetaSVM (Dong *et al*, 2015). Either loss of function mutations of stop-gains, stop-losses, frameshift indels, and canonical splice-sites or deleterious missense mutations predicted by MetaSVM were considered to potentially damaging. Recessive variants of which MAF values in Genome Aggregation Database (gnomeAD), v2.1 (Lek *et al*, 2016; https://gnomad.broadinstitute.org/) are lower than 10^{-3} were considered for rare variants. Rare damaging variants were further filtered to exclude false-

positives using the follow criteria: (1) PASS for GATK variant quality score recalibration, (2) MAF ≤ 2.0 x 10^{-5} in the gnomAD, (3) DP ≥ 8 independent reads, (4) GC score ≥ 20, (5) MQ score ≥ 40, (6) PLdiff/DP ≥ 8, and (7) indels in Low Complexity Regions. Co-segregation of candidate variants with the phenotypes were confirmed by genomic DNA PCR and Sanger sequencing. Genomic DNA PCR was performed with using One*Taq*® 2X Master Mix (NEB) and used primer pairs were; Fwd: 5'-GCTGAGCATTTGGAGTGGC-3' and Rev: 5'-CCTGCTAGGTGGCTGTGTAT-3' for *LRRC23*, Fwd: 5'-TGAACCCCTGGCACAACT-3' and Rev: 5'-TTTTTACTCAGCGATACCACATTCACAG-3' for *SCN5A*, Fwd: 5'-TGGCTAAATCCCATCCAGTCC-3' and Rev: 5'- GAGTCTGTCCTTGCCCGTAG-3' for *NOX1,* and Fwd: 5'-GATTGTCATCGCCTTGTTCATC-3' and Rev: 5'-TGTTTTGTGGTGGCACAGTC-3' for *PRRG3*. Amplified PCR products were subjected to Sanger sequencing.

Kinship Analysis

Kinship coefficient was estimated to confirm pedigree information and pairwise relatedness of proband using KING v2.2.4 (Manichaikul *et al*, 2010). Inbreeding coefficient was calculated by homozygosity-by-descent (HBD). HBD segment in the proband was detected by Beagle v3.3.2 (Browning & Browning, 2011). Homozygosity in segments over 2 cM was considered for consanguinity.

Animals

Wildtype C57BL/6 mice were from Charles River Laboratory. Mice were cared in accordance with the guidelines approved by Institutional Animal Care and Use Committee (IACUC) for Yale University (#20079).

Generation of the *Lrrc23*-mutant mice and genotyping

Lrrc23-mutant mice were generated on C57BL/6 background using CRISPR/Cas9 genome editing as described (Chen *et al*, 2016; Yang *et al*, 2014). Two guide RNAs targeting the 5th (5'-CATATGGTAACATTGACCCAGGG-3') and 7th (5'- CGTCTCTACCAGCTATACAGCGG-3') were *in vitro* transcribed and purified. The sgRNAs/Cas9 RNPs were complexed and electroporated into zygotes from C57BL/6J. The embryos were transplanted to oviducts of pseudopregnant CD-1 foster females and founders' toe were biopsied to extract gDNA. Truncation of the target region was confirmed by gDNA PCR with F3 (5'-CACTTTTCCTGCCTCTGTGTCC-3') and R3 (5'-AGCATCTCCCACTTCCTGTGAC-3') primers. The amplicons were Sanger sequenced and founder females with 4126bp or 4128bp truncation at the genomic region (*4126del* and *4135del*) were mated with C57BL/6 WT mice to confirm the germline transmission of the alleles. Two mutant mice lines were maintained and genotyped with F3-R3 pairs for the mutant allele and F2 (5'-TTGTGGTGGTGGGGAGATAG-3')-R2 (5'-GTGGTGATGGACGGGTGT-3') pair for WT allele.

Mouse sperm preparation

Sperm were collected from cauda epididymis of the adult mice by swim-out in M2 medium (EMD Millipore). To induce capacitation, the epididymal sperm were incubated in human tubular fluid (HTF; EMD Millipore) at 2.0 x 10^6 cells/ml concentration for 90 minutes at 37 °C, 5% CO_2 condition.

Mammalian Cell culture and transient protein expression

Human embryonic kidney 293T cells (ATTC) were cultured in DMEM (Gibco) supplemented with 10% FBS (Gibco) and 1X Pen/Strep (Gibco) at 37 °C, 5% CO_2 condition. Cultured cells were

transfected with Lipofectamine 2000 (Invitrogen) or polyethylenimine (PEI) to express recombinant protein transiently. Transfected cells were used for co-immunoprecipitation or modified trap-assay.

RNA extraction, cDNA synthesis, and PCR

Total RNA was extracted from transfected 293T cells and frozen mouse testes using RNeasy Mini kit (QIAGEN). Extracted RNA was used for cDNA synthesis using iScript cDNA Synthesis kit (BIO-RAD) in accordance with manufacturer's instruction. Synthesized testis cDNAs were used for endpoint PCR or quantitative PCR using OneTaq 2X Master Mix (NEB) or with iTaq Universal SYBR Green Supermix (BIO-RAD), respectively. Primer pairs, F1 (5'-GGCATCTCTCATCCTCGTCT-3') - R1 (5'-AGCCACTCAGGGTGTCAATC-3'), F4 (5'-TTGGCGTCTCAGCACAAAG-3') - R4 (5'-CTCGAAGCTCCAGGGTGT-3'), and F5 (5'-CTGGACCCCGAGAGACTG-3') - R5 (5'-AGTTTTACCCCCGACCTGTG-3') were used for endpoint PCR; E3 (5'-AGCTGGAGGCTAAGGACAGG-3') - E4 (5'-GAGCGGCGATATGTCTGTAA-3') and E7 (5'-GTCAGAGGCTGAAGGAGGAA-3') - E8 (5'-TATCAGTTCTTGGGGCCAGT-3') were used for quantitative PCR. TBP was used to calculate relative transcript levels in mouse testes by ΔΔCt method.

Antibodies and reagent

Rabbit polyclonal RSPH3B were described in previous studies (Hwang *et al.*, 2021b). Rabbit polyclonal anti-LRRC23 (α-118, PA5-63449; α-208, PA5-58095), DNAH1 (PA5-57826), DNAH2 (PA5-64309), and DNAH9 (PA5-45744) were from Invitrogen. Rabbit polyclonal SEPTIN4 (NBP1-90093) antibody was from Novus Biologicals. Mouse monoclonal anti-His-tag (66005-1-Ig) and rabbit polyclonal anti-AKAP3 (13907-1-AP), RSPH9 (23253-1-AP), and RSPH22 (16811-1-AP) were purchased from Proteintech. Rabbit polyclonal TOM20 (sc-11415) was from SantaCruz. Mouse monoclonal anti-acetylated tubulin (AcTub, clone 6-11B-1, 7451), CALM1 (05-173), pTyr (clone 4G10, 05-321), and HA (clone HA-7, H3663) and rabbit polyclonal anti-SEPTIN12 (HPA041128) were from Sigma-Aldrich. Rabbit and mouse monoclonal anti-DYKDDDDK (clone D6W5B, 86861; clone 9A3, 8146) were from Cell Signaling Technology. Rabbit polyclonal ODF2 and AKAP4 were gifted from Dr. Edward M. Eddy. Rabbit anti-RSPH6A sera was gifted from Dr. Masahito Ikawa. HRP-conjugated goat anti-mouse and anti-rabbit IgG were from Jackson ImmunoResearch. Goat anti-rabbit IgG conjugated with Alexa 568, Lectin PNA conjugated with Alexa 647, and Hoechst dye were from Invitrogen.

Protein extraction, solubilization, and immunoblotting

Testis Adult mouse testes were homogenized in 0.32M using dounce homogenizer followed by centrifugation for 15 minutes at 4 °C, 1000 x g to pellet nucleus and debris. Supernatants was collected and centrifuged at 4 °C, 100,000 rpm for an hour to separate cytosolic and microsome fractions. Volume-equivalented cytosolic and microsome fractions were lysed with 2X LDS sampling buffer and denatured by boiling at 75 °C with 50 mM dithiothreitol (DTT) for 2 or 10 minutes, respectively, for SDS-PAGE and immunoblotting. Primary antibodies used for immunoblotting were: rabbit polyclonal anti-LRRC23 (α-118 and α-208, both 1:500) and mouse monoclonal anti-AcTub (1:2,000), and calmodulin (1:1,000).

Epididymal sperm Collected epididymal cells were washed with PBS and lysed using 2X LDS by vortexing at room temperature (RT) for 10 minutes to extract whole sperm proteins as described previously (Hwang et al., 2022). The lysates were centrifuged for 10 minutes at 4 °C, 18,000 x g and the supernatant were mixed to 50 mM DTT followed by boiling at 75 °C for 10

minutes for denaturation. The samples were subjected to SDS-PAGE and immunoblotting. The used primary antibodies were: rabbit polyclonal anti-LRRC23 (α-118 and α-208, 1:500), AKAP3 (1:2,000), RSPH9 (1:500), RSPH22 (1:1,000), ODF2 (1:2,000), AKAP4 (1:2,000), and RSPH3 (1:500), rabbit anti-RSPH6A sera (1:500), and mouse monoclonal AcTub (1:20,000).

293T cells 293T cells were lysed using 0.5% Triton X-100 in 10 mM HEPES, 140 mM NaCl, pH7.4 buffer (1X HEPES buffer) for 2 hours at 4 °C with gentle rocking. The lysates were centrifuged at 4 °C, 18,000 x g for 30 minutes. Supernatant with solubilized proteins were used for protein interaction tests or mixed to 1X LDS and 50 mM DTT followed by boiling at 75 °C for 2 minutes. Denatured samples were used for immunoblotting. Mouse monoclonal anti-HA (1:4000) and FLAG (1:1000), and rabbit monoclonal anti-FLAG (1:1000) were used for primary antibody. HRP-conjugated goat anti-rabbit and goat anti-mouse IgG were used for secondary antibodies (0.1 μg/ml). SuperSignal™ Western Blot Enhancer (Thermo Scientific) was used for testis and sperm immunoblotting with anti-LRRC23 antibody (α-118).

Molecular cloning

Human *LRRC23* ORF clone (HG24717-UT, SinoBiological) and the partial region of the human *LRRC23* 5th intron amplified by PCR was subcloned into phCMV3 vector to generate mammalian expression constructs for human *LRRC23* (*phCMV3-FLAG-hLRRC23^{ORF}-HA*, *phCMV3-FLAG-hLRRC23^{WT}-HA,* and *phCMV3-FLAG-hLRRC23^{Mut}-HA*). cDNA clones of human *RSPH3* (616166, Horizon Discovery), *RSPH6A* (5270908, Horizon Discovery), *RSPH9* (5296237, Horizon Discovery), and *RSPH22* (OHu31347, GenScript) was subcloned into *phCMV3* to express human RSPH proteins tagged with FLAG at C-termini. A stop codon was placed at the upstream of sequences encoding HA in phCMV3 vector for tagging FLAG at C-termini. ORFs encoding full-length and the predicted mutant LRRC23 were amplified from *phCMV3-FLAG-hLRRC23^{ORF}-HA* constructs and subcloned into *pGEX-6P2* vector to generate *pGEX-6P2-hLRRC23^{WT}* and *pGEX-6P2-hLRRC23^{Mut}* constructs tagging with HA at C-termini. ORFs for each construct were amplified using Q5 Hot Start High-Fidelity 2X Master Mix (NEB) and subcloned into linear vectors using NEBuilder HiFi DNA Assembly Kit (NEB)

Recombinant protein purification

Bacterial expression constructs were transformed to BL21-CodonPlus(DE3)-RIL competent cells (Agilent Technologies). Fresh colonies were cultured into LB with antibiotics overnight at 37 °C and cultured further after 50 times dilution at 37 °C until OD_{600} values reach to 0.5-0.8. The cultivates were treated with 1mM IPTG to express recombinant proteins and cultured further for 16-18 hours at 16 °C. IPTG-treated bacteria were washed with PBS and eluted with 1X HEPES buffer containing 1% Triton X-100 and EDTA-free protease inhibitor cocktail (Roche) The elutes were sonicated and centrifuged at 18,000 x g, 4 °C for 1 hour. Supernatant were collected and incubated with glutathione agarose (Pierce) for overnight at 4 C to purify recombinant GST and GST-tagged human LRRC23^{WT} and LRRC23^{Mut}. The incubated resins were washed with PBS and eluted with 1X HEPES buffer supplemented with 10 mM reduced glutathione. The elutes were dialyzed against 1X HEPES buffer with 50% glycerol for overnight at 4 °C. Purified proteins were subjected to Coomassie gel staining using Imperial™ Protein Stain (Thermo Scientific) and immunoblotting.

Modified trap assay

293T cells to express FLAG-tagged human RSPH proteins transiently were lysed with 1% Triton X-100 in 1X HEPES buffer with EDTA-free protease inhibitor cocktail (Roche) by rocking at 4 °C

for 2 hours. The lysates were centrifuged at 18,000 x g for 30 minutes at 4 °C and the supernatant was incubated with Surebeads^{TM} Protein A Magnetic Bead (Bio-rad) conjugated with rabbit monoclonal DYKDDDDK antibody at RT for two hours. The magnetic beads were washed with 1% Triton X-100 in 1X HEPES buffer two times and 0.2% Triton X-100 in 1X HEPES buffer. Purified GST, GST-tagged human LRRC23^{WT} and LRRC23^{Mut} proteins were incubated with the washed magnetic beads in 0.2% Triton X-100 in 1X HEPES buffer at 4 °C for overnight. Incubated magnetic beads were washed with 0.2% Triton X-100 in 1X HEPES buffer for three times and eluted with 2X LDS buffer containing 50 mM DTT followed by denatured 75 °C for 10 minutes.

Sperm fluorescence staining

Epididymal sperm cells were washed with PBS and attached on the glass coverslips by centrifugation at 700 x g for 5 minutes. The coverslips were fixed with either 4% PFA in PBS at RT for 10 minutes (SEPTIN4, SEPTIN12, RSPH3, DNAH2, DNAH9, TOM20, and LRRC23) or acetone at – 20 °C for 5 minutes (RSPH9, DNAH1, AKAP4, ODF2, and AcTub). PFA fixed coverslips were washed with PBS three times and permeablized with 0.1% (SEPTIN4 and SEPTIN12), 0.5% (RSPH3, LRRC23, and DNAH9), or 1% (DNAH2) Triton X-100 in PBS at RT for 10 minutes. Acetone-fixed coverslips were rehydrated by washing with 0.1% Triton X-100 in PBS and PBS. Permeablized coverslips were blocked with 10 % normal goat serum in PBS and incubated with primary antibodies in blocking buffer at 4 °C overnight. Used primary antibodies were: Rabbit polyclonal anti-LRRC23 (α-118, 1:100), SEPTIN4 (1 μg/ml), SEPTIN12 (1:100), RSPH3 (10 μg/ml), RSPH9 (1:100), DNAH1 (3 μg/ml), DNAH2 (0.5 μg/ml), DNAH9 (5 μg/ml), TOM20 (1:50), AKAP4 (1:100), and ODF2 (1:50), and mouse monoclonal anti-AcTub (1:200). Coverslips were washed with 0.1% Triton X-100 in PBS one time and PBS two times and incubated with either goat anti-rabbit or mouse IgG conjugated with Alexa 568 in blocking buffer at RT for an hour. The coverslips were washed with PBS three times and mounted on the glass slide using Vectasheild (Vector Laboratory). To observe sperm acrosome, PFA-fixed coverslips were incubated with PNA conjugated with Alexa 647 at RT for an hour. Fluorescence stained coverslips were imaged using Zeiss LSM710 Elyra P1 with Plan-Apochrombat 63X/1.40 objective (Carl Zeiss). Hoechst were used for counter staining.

Mating test

Adult heterozygous and homozygous *Lrrc23* mutant male mice were housed with adult female mice with normal fertility and monitored over two months. The pregnancy and litter size were recorded.

Sperm motility analysis

Computer-assisted sperm analysis Computer-assisted sperm analysis (CASA) was performed as previous study (Hwang *et al*, 2022)**.** Briefly, sperm cells at 3.0 x 10^6 cells/ml concentration were loaded in slide chamber (CellVision) and their motility parameters were measured on 37 °C warm-stage. Motility of over 200 sperm was recorded using CMOS video camera (Basler acA1300-200μm, Basler AG) at 50 frame per seconds (fps) through 10x phase contrast objective (CFI Plan Achro 10X/0.25 Ph1 BM, Nikon) equipped in Nikon E200 microscope. The recorded sperm motility was analyzed using Sperm Class Analyzer software (Microptic).

Sperm swimming path analysis Sperm free swimming analysis was conducted as previous study (Hwang *et al*, 2019; Hwang *et al*, 2021a). Briefly, sperm cells were transferred to

Delta-T culture dish controller (Bioptech) filled with 37 °C HEPES-buffered HTF medium with 0.3% methylcellulose (Chung *et al*, 2017). Sperm swimming was imaged using pco.edge sCMOS camera in Axio observer Z1 microscope (Carl Zeiss) for 2 seconds with 100 fps. FIJI software (Schindelin *et al*, 2012) was used to generate overlaid images to show sperm swimming paths.

Flagellar waveform analysis To analyze sperm flagellar waveform, 2.0 x 10^5 cells of capacitated and non-capacitated sperm cells were placed into 37 °C HEPES-buffered HTF medium (Chung *et al.*, 2017) in fibronectin-coated Delta-T culture dish controller (Bioptech). Flagellar movement of the head-tethered sperm was recorded using pco.edge sCMOS camera equipped in Axio observer Z1 microscope (Carl Zeiss) for 2 seconds with 200 fps. Recorded image stacks were applied to generate overlaid images to show flagellar waveform for two beating cycles with FIJI software (Schindelin *et al.*, 2012).

Sequence alignment and phylogenetic analysis

Amino acid sequences of human and mouse normal and mutant LRRC23 were aligned using Clustal Omega (https://www.ebi.ac.uk/Tools/msa/clustalo/). Amino acids sequences of LRRC23 and LRRC34 orthologs and *Chlamydomonas reinhardtii* RSP15 were aligned with ClustalW for phylogenetic analysis using MEGA7 (Kumar *et al*, 2016). Pairwise distances between the sequences were calculated with default option. An unrooted phylogenetic tree was generated by maximum-likelihood analysis with 500 bootstrap replications.

Protein structure analysis

Radial spoke 2 and RSP15 structures of the *C. reinhardtii* were from RCSC Protein Data Bank, PDB (https://www.rcsb.org/; 7JU4). Predicted structures of human LRRC23 (Q53EV4) and LRRC34 (Q8IZ02) were from AlphaFold Protein Structure Database (Jumper *et al*, 2021; https://alphafold.ebi.ac.uk/). Protein structures were rendered and visualized by Mol* 3D Viewer at RCSC PDB.

Tissue and testicular expression analysis

Transcript expression data of *LRRC23* and *LRRC34* in human tissues was obtained from GTEx and is based on The Human Protein Atlas version 21.0 and Ensembl version 103.38 (https://www.proteinatlas.org/about/download). Medians of the normalized transcript per million (nTPM) are used to calculate relative tissue expression levels. Relative tissue expression levels of *LRRC23* and *LRRC34* are represented as heatmap using GraphPad Prism 8.0 (GraphPad Software Inc., San Diego, CA). UMAP images for the single-cell expression of *LRRC23* and *LRRC34* in human testis are obtained from UCSC Cell browser (Soraggi *et al*, 2021; https://cells.ucsc.edu/?ds=testis).

Transmission electron microscopy

Transmission electron microscopy was performed as previous study (Hwang *et al.*, 2021b). Washed epididymal sperm were pelleted by centrifugation and fixed with 2.5% glutaraldehyde and 2% paraformaldehyde in 0.1M cacodylate buffer pH7.0 for 30 minutes at RT and for 1 hour at 4 °C. The fixed pellets were briefly washed with 0.1M cacodylate buffer pH7.0 and placed in 2% agar. The chilled blocks were trimmed and rinsed with 0.1M cacodylate buffer followed by placed in 0.1% tannic acid in 0.1M cacodylate buffer for 1 hour. The samples were washed and post-fixed in 1% osmium tetroxide and 0.15% potassium ferrocyanide in 0.1M cacodylate buffer for 1 hour. Post-fixed samples were rinsed with the cacodylate buffer and distilled water and subjected to en bloc staining in 2% aqueous uranyl acetate for 1 hour. The samples were dehydrated with

ethanol series and infiltrated with epoxy resin Embed 812 (Electron Microscopy Scienes). The resins were placed in silicone molds and backed for 24 hours at 60 °C. The blocks were sectioned in 60 nm depth using Leica UltraCut UC7 and the sections were collected on the formvar/carbon-coated grids. Sections on the grids were stained using 2% uranyl acetate and lead citrate. The stained grids were imaged using MORADA CCD camera (Olympus) equipped in FEI Tecnai Biotwin Transmission Electron Microscope (FEI, Hillsboro, OR) at 80 KV.

Cryo-electron tomography

Grid preparation Grids for sample imaging were prepared as a previously report (Leung *et al.*, 2021). The Quantifoil R2/2 gold grids were glow discharged for 30 seconds at 15mA and 1.5 x 10^5 cells of WT or *Lrrc23*$^{\Delta/\Delta}$ sperm were loaded on the grids followed by incubation at RT for 1 minutes. The grids were blotted manually from the back site for ~4 seconds using a manual plunger freezer and immediately plunged into liquid ethane and stored in liquid nitrogen.

Cryo-ET data collection Prepared grids with proper ice particles were screened using a Glacios microscope (200 KV, ThermoFisher Scientific) at the Yale Science Hill Electron Microscopy Facility. The screened grids were transferred to the Titan Krios microscope (300 KV, ThermoFisher Scientific) equipped with a Bioquantum Energy Filter and a K3 direct electron detector (Gatan) for data collection at the Yale West Campus Electron Microscopy Facility. Data was collected automatically using SerialEM (Mastronarde, 2005). All images were recorded under super-resolution mode with the physical pixel size 3.4 Å (1.7 Å for super resolution movies). 20 and 60 tilt series of WT and *Lrrc23*$^{\Delta/\Delta}$ mouse sperm were collected with the Volta phase plate at a target defocus around -1 µm. Grouped dose-symmetric scheme spanning from -51° to 51° at 3° increment was applied for tilt series acquisition, with a total dose at 100e-/Å2.

Tomogram reconstruction Process of tomogram reconstruction was streamlined using in-house scripts. The movie frames were aligned first using MotionCorr2 and the micrographs were binned with a factor two (Zheng *et al*, 2016). Tilt series stack was generated using in-house script. The tilt-series was aligned by AreTomo 1.0.6 (Zheng *et al*, 2022) to generate XF files which are comparable for IMOD (Kremer *et al*, 1996). The initial CTF parameters were estimated using Ctffind4 (Rohou & Grigorieff, 2015). The tomograms were then reconstructed with a binning factor six with 20.4 Å pixel size by IMOD with SIRT algorithm for visualization, particle picking and initial sub-tomogram averaging.

Sub-Tomogram Averaging of 96-nm axonemal doublet repeat

Initial alignment using PEET MTDs were manually traced in IMOD (Kremer *et al.*, 1996). After manual tracing, a polynomial function with degree five was fitted to each microtubule doublet with 24 nm of a sampling distance (Fig EV6C). The polarity of each tomogram is manually determined to reduce the error during subsequent alignment. The 24-nm repeat particles were first aligned using PEET Version 1.15.0 under “Particle model points” and “align particle Y axes” options (Heumann *et al*, 2011; Nicastro *et al*, 2006). A published map of 96-nm MTD repeat in WT mouse sperm (EMD-12133; Leung *et al.*, 2021) was low-pass filtered to 60 Å and used as the initial reference. A mask covering two adjacent MTDs was generated with 160 x 160 x 160 nm^3 dimension of sub-tomogram particle. Only “Phi” angle and translational shifts were searched during the alignment. After the initial alignment, positions of the particles were placed at center based on the translational shifts. The Euler angles were extracted and transformed to RELION Euler angle convention (ZYZ) using the MOTL2Relion command in PEET. In-house script was used to gather the coordinates and corresponding Euler angle information for subsequent RELION4 sub-tomogram averaging analysis.

Refinement and classification After the metadata preparation, the sub-tomogram particles were made in RELION4 (Zivanov *et al*, 2022) with the binning factor of six. Local 3D refinement with a mask covering one 96-nm MTD was performed. After refinement, the features pf 24-nm repeat of outer dynein arm was observed (Fig EV6D). A smaller mask only covering the inner dynein arm and radial spoke was created for the focused classification without alignment (Fig EV6E). After classification, equivalent 96-nm MTD repeat classes were separated (Fig EV6E). One of the classes was selected for the future process. New sub-tomogram particles with binning factor three and corresponding 10.2 Å of pixel size were generated. Another local refinement was performed with a 96-nm MTD mask. Resolution was estimated using the Fourier shell correlation (FSC) at a cut-off of 0.143 in RELION4 (Zivanov *et al.*, 2022). Details of acquisition parameters and particle numbers are summarized in Table EV3.

Visualization Images for cryo-ET and sub-tomogram averaging were rendered using IMOD (Kremer *et al.*, 1996) and UCSF Chimerax (Goddard *et al*, 2018).

Statistical analysis

Statistical analyses were performed using Student's t-test or Mann-Whitney U test. Significant differences were considered at *$p \leq 0.05$, **$p < 0.01$, and ***$p < 0.001$.

Data availability

The structures for radial spokes from WT (EMD-29013) and *LRRC23*$^{\Delta/\Delta}$ (EMD-28606) sperm resolved by cryo-ET and STA are deposited to Electron Microscopy Data Bank (https://ebi.ac.uk/pdbe/emdb).

Acknowledgments

The authors highly appreciate participation of the family members in the study presented here. We also thank Muhammad Umair, Khadim Shah, Imran Ullah, Hammal Khan for their help to visit the family for interviews and participation in clinical assessment, Habibur Rehmen and Rina Raza from Aga Khan Medical Centre for clinical semen analyses, Jong-Nam Oh for preparing samples for WES, Case Porter and Miriam Hill for their help in PCR and Sanger sequencing, the Yale Center for Cellular and Molecular Imaging for assistance in transmission electron microscopy, Dr. Masahito Ikawa from Osaka University for sharing anti-RSPH6A sera. This study was supported by start-up funds from Yale University School of Medicine and National Institute of Child Health and Human Development (R01HD096745) to J-JC; start-up funds from Yale University, National Institute of General Medical Sciences (R35GM142959) to KZ; Pakistan Academy of Sciences (PAS-171) to WA; National Human Genome Research Institute (UM1HG006504) to the Yale Center for Mendelian Genomics. JH was in part supported by Postdoctoral Fellowship from MCI. SN was supported by Pakistan Higher Education Commission International Research Support Initiative Program. JC was in part supported by a Korea University Medical Center Grant. The Genome Sequencing Program Coordinating Center (U24 HG008956) contributed to cross-program scientific initiatives and provided logistical and general study coordination.

Author Contributions

Jae Yeon Hwang: Conceptualization; methodology; formal analysis; data curation; writing - original draft; writing – review and editing. **Pengxin Chai:** Methodology; formal analysis; data curation; writing – original draft. **Shoaib Nawaz:** Investigation; methodology; formal analysis. **Jungmin Choi:** Methodology; formal analysis; data curation. **Francesc Lopez-Giraldez:** Methodology; formal analysis; data curation. **Shabir Hussain:** Investigation. **Kaya Bilguvar;** Formal analysis. **Shrikant Mane:** Formal analysis. **Richard P. Lifton;** Resource. **Wasim Ahmad:** Resource. **Kai Zhang:** Conceptualization; formal analysis; writing – review and editing; resource; funding acquisition. **Jean-Ju Chung:** Conceptualization; formal analysis; data curation; writing - original draft; writing – review and editing; resource; supervision; funding acquisition.

Disclosure and competing interests statement

The authors declare that they have no conflict of interest.

References

Abbasi F, Miyata H, Shimada K, Morohoshi A, Nozawa K, Matsumura T, Xu Z, Pratiwi P, Ikawa M (2018) RSPH6A is required for sperm flagellum formation and male fertility in mice. *J Cell Sci* 131

Auguste Y, Delague V, Desvignes JP, Longepied G, Gnisci A, Besnier P, Levy N, Beroud C, Megarbane A, Metzler-Guillemain C *et al* (2018) Loss of Calmodulin- and Radial-Spoke-Associated Complex Protein CFAP251 Leads to Immotile Spermatozoa Lacking Mitochondria and Infertility in Men. *Am J Hum Genet* 103: 413-420

Bazan R, Schrofel A, Joachimiak E, Poprzeczko M, Pigino G, Wloga D (2021) Ccdc113/Ccdc96 complex, a novel regulator of ciliary beating that connects radial spoke 3 to dynein g and the nexin link. *PLoS Genet* 17: e1009388

Browning BL, Browning SR (2011) A fast, powerful method for detecting identity by descent. *The American Journal of Human Genetics* 88: 173-182

Castleman VH, Romio L, Chodhari R, Hirst RA, de Castro SC, Parker KA, Ybot-Gonzalez P, Emes RD, Wilson SW, Wallis C *et al* (2009) Mutations in radial spoke head protein genes RSPH9 and RSPH4A cause primary ciliary dyskinesia with central-microtubular-pair abnormalities. *Am J Hum Genet* 84: 197-209

Cavarocchi E, Whitfield M, Saez F, Toure A (2022) Sperm Ion Transporters and Channels in Human Asthenozoospermia: Genetic Etiology, Lessons from Animal Models, and Clinical Perspectives. *Int J Mol Sci* 23

Chen S, Lee B, Lee AY-F, Modzelewski AJ, He L (2016) Highly efficient mouse genome editing by CRISPR ribonucleoprotein electroporation of zygotes. *Journal of Biological Chemistry* 291: 14457-14467

Chen Z, Greenan GA, Shiozaki M, Liu Y, Skinner WM, Zhao X, Zhao S, Yan R, Yu Z, Lishko PV *et al* (2023) In situ cryo-electron tomography reveals the asymmetric architecture of mammalian sperm axonemes. *Nat Struct Mol Biol* 30: 360-369

Chung JJ, Miki K, Kim D, Shim SH, Shi HF, Hwang JY, Cai X, Iseri Y, Zhuang X, Clapham DE (2017) CatSperzeta regulates the structural continuity of sperm Ca(2+) signaling domains and is required for normal fertility. *Elife* 6

Curi SM, Ariagno JI, Chenlo PH, Mendeluk GR, Pugliese MN, Sardi Segovia LM, Repetto HE, Blanco AM (2003) Asthenozoospermia: analysis of a large population. *Arch Androl* 49: 343-349

Dong C, Wei P, Jian X, Gibbs R, Boerwinkle E, Wang K, Liu X (2015) Comparison and integration of deleteriousness prediction methods for nonsynonymous SNVs in whole exome sequencing studies. *Human molecular genetics* 24: 2125-2137

Goddard TD, Huang CC, Meng EC, Pettersen EF, Couch GS, Morris JH, Ferrin TE (2018) UCSF ChimeraX: Meeting modern challenges in visualization and analysis. *Protein Sci* 27: 14-25

Gui M, Ma M, Sze-Tu E, Wang X, Koh F, Zhong ED, Berger B, Davis JH, Dutcher SK, Zhang R *et al* (2021) Structures of radial spokes and associated complexes important for ciliary motility. *Nat Struct Mol Biol* 28: 29-37

Han X, Xie H, Wang Y, Zhao C (2018) Radial spoke proteins regulate otolith formation during early zebrafish development. *FASEB J* 32: 3984-3992

Heumann JM, Hoenger A, Mastronarde DN (2011) Clustering and variance maps for cryo-electron tomography using wedge-masked differences. *J Struct Biol* 175: 288-299

Hwang JY, Mannowetz N, Zhang Y, Everley RA, Gygi SP, Bewersdorf J, Lishko PV, Chung JJ (2019) Dual Sensing of Physiologic pH and Calcium by EFCAB9 Regulates Sperm Motility. *Cell* 177: 1480-1494 e1419

790 Hwang JY, Maziarz J, Wagner GP, Chung JJ (2021a) Molecular Evolution of CatSper in Mammals
791 and Function of Sperm Hyperactivation in Gray Short-Tailed Opossum. *Cells* 10
792 Hwang JY, Nawaz S, Choi J, Wang H, Hussain S, Nawaz M, Lopez-Giraldez F, Jeong K, Dong W, Oh
793 JN *et al* (2021b) Genetic Defects in DNAH2 Underlie Male Infertility With Multiple Morphological
794 Abnormalities of the Sperm Flagella in Humans and Mice. *Front Cell Dev Biol* 9: 662903
795 Hwang JY, Wang H, Lu Y, Ikawa M, Chung JJ (2022) C2cd6-encoded CatSpertau targets sperm
796 calcium channel to Ca(2+) signaling domains in the flagellar membrane. *Cell Rep* 38: 110226
797 Imhof S, Zhang J, Wang H, Bui KH, Nguyen H, Atanasov I, Hui WH, Yang SK, Zhou ZH, Hill KL
798 (2019) Cryo electron tomography with volta phase plate reveals novel structural foundations of
799 the 96-nm axonemal repeat in the pathogen Trypanosoma brucei. *Elife* 8
800 Inaba K (2011) Sperm flagella: comparative and phylogenetic perspectives of protein
801 components. *Mol Hum Reprod* 17: 524-538
802 Ishikawa T (2017) Axoneme Structure from Motile Cilia. *Cold Spring Harb Perspect Biol* 9
803 Jeanson L, Copin B, Papon JF, Dastot-Le Moal F, Duquesnoy P, Montantin G, Cadranel J, Corvol H,
804 Coste A, Desir J *et al* (2015) RSPH3 Mutations Cause Primary Ciliary Dyskinesia with Central-
805 Complex Defects and a Near Absence of Radial Spokes. *Am J Hum Genet* 97: 153-162
806 Jumper J, Evans R, Pritzel A, Green T, Figurnov M, Ronneberger O, Tunyasuvunakool K, Bates R,
807 Zidek A, Potapenko A *et al* (2021) Highly accurate protein structure prediction with AlphaFold.
808 *Nature* 596: 583-589
809 Kherraf ZE, Amiri-Yekta A, Dacheux D, Karaouzene T, Coutton C, Christou-Kent M, Martinez G,
810 Landrein N, Le Tanno P, Fourati Ben Mustapha S *et al* (2018) A Homozygous Ancestral SVA-
811 Insertion-Mediated Deletion in WDR66 Induces Multiple Morphological Abnormalities of the
812 Sperm Flagellum and Male Infertility. *Am J Hum Genet* 103: 400-412
813 Knowles MR, Ostrowski LE, Leigh MW, Sears PR, Davis SD, Wolf WE, Hazucha MJ, Carson JL,
814 Olivier KN, Sagel SD *et al* (2014) Mutations in RSPH1 cause primary ciliary dyskinesia with a
815 unique clinical and ciliary phenotype. *Am J Respir Crit Care Med* 189: 707-717
816 Kott E, Legendre M, Copin B, Papon JF, Dastot-Le Moal F, Montantin G, Duquesnoy P, Piterboth
817 W, Amram D, Bassinet L *et al* (2013) Loss-of-function mutations in RSPH1 cause primary ciliary
818 dyskinesia with central-complex and radial-spoke defects. *Am J Hum Genet* 93: 561-570
819 Krause I, Pohler U, Grosse S, Shebl O, Petek E, Chandra A, Ebner T (2016) Characterization of the
820 injection funnel during intracytoplasmic sperm injection reflects cytoplasmic maturity of the
821 oocyte. *Fertil Steril* 106: 1101-1106
822 Kremer JR, Mastronarde DN, McIntosh JR (1996) Computer visualization of three-dimensional
823 image data using IMOD. *J Struct Biol* 116: 71-76
824 Kubo S, Yang SK, Black CS, Dai D, Valente-Paterno M, Gaertig J, Ichikawa M, Bui KH (2021)
825 Remodeling and activation mechanisms of outer arm dyneins revealed by cryo-EM. *EMBO Rep*
826 22: e52911
827 Kumar S, Stecher G, Tamura K (2016) MEGA7: Molecular Evolutionary Genetics Analysis Version
828 7.0 for Bigger Datasets. *Mol Biol Evol* 33: 1870-1874
829 Lek M, Karczewski KJ, Minikel EV, Samocha KE, Banks E, Fennell T, O'Donnell-Luria AH, Ware JS,
830 Hill AJ, Cummings BB (2016) Analysis of protein-coding genetic variation in 60,706 humans.
831 *Nature* 536: 285-291
832 Leung MR, Roelofs MC, Ravi RT, Maitan P, Henning H, Zhang M, Bromfield EG, Howes SC,
833 Gadella BM, Bloomfield-Gadelha H *et al* (2021) The multi-scale architecture of mammalian
834 sperm flagella and implications for ciliary motility. *EMBO J* 40: e107410

835 Li H (2013) Aligning sequence reads, clone sequences and assembly contigs with BWA-MEM.
836 *arXiv preprint arXiv:13033997*
837 Lin J, Heuser T, Carbajal-Gonzalez BI, Song K, Nicastro D (2012) The structural heterogeneity of
838 radial spokes in cilia and flagella is conserved. *Cytoskeleton (Hoboken)* 69: 88-100
839 Lin J, Yin W, Smith MC, Song K, Leigh MW, Zariwala MA, Knowles MR, Ostrowski LE, Nicastro D
840 (2014) Cryo-electron tomography reveals ciliary defects underlying human RSPH1 primary ciliary
841 dyskinesia. *Nat Commun* 5: 5727
842 Liu S, Zhang J, Kherraf ZE, Sun S, Zhang X, Cazin C, Coutton C, Zouari R, Zhao S, Hu F *et al* (2021)
843 CFAP61 is required for sperm flagellum formation and male fertility in human and mouse.
844 *Development* 148
845 Ma A, Zeb A, Ali I, Zhao D, Khan A, Zhang B, Zhou J, Khan R, Zhang H, Zhang Y *et al* (2021) Biallelic
846 Variants in CFAP61 Cause Multiple Morphological Abnormalities of the Flagella and Male
847 Infertility. *Front Cell Dev Biol* 9: 803818
848 Manichaikul A, Mychaleckyj JC, Rich SS, Daly K, Sale M, Chen W-M (2010) Robust relationship
849 inference in genome-wide association studies. *Bioinformatics* 26: 2867-2873
850 Martinez G, Beurois J, Dacheux D, Cazin C, Bidart M, Kherraf ZE, Robinson DR, Satre V, Le Gac G,
851 Ka C *et al* (2020) Biallelic variants in MAATS1 encoding CFAP91, a calmodulin-associated and
852 spoke-associated complex protein, cause severe astheno-teratozoospermia and male infertility.
853 *J Med Genet* 57: 708-716
854 Mastronarde DN (2005) Automated electron microscope tomography using robust prediction of
855 specimen movements. *J Struct Biol* 152: 36-51
856 McKenna A, Hanna M, Banks E, Sivachenko A, Cibulskis K, Kernytsky A, Garimella K, Altshuler D,
857 Gabriel S, Daly M (2010) The Genome Analysis Toolkit: a MapReduce framework for analyzing
858 next-generation DNA sequencing data. *Genome research* 20: 1297-1303
859 Nawaz S, Ullah MI, Hamid BS, Nargis J, Nawaz M, Hussain S, Ahmad W (2021) A loss-of-function
860 variant in DNA mismatch repair gene MLH3 underlies severe oligozoospermia. *J Hum Genet* 66:
861 725-730
862 Nicastro D, Schwartz C, Pierson J, Gaudette R, Porter ME, McIntosh JR (2006) The molecular
863 architecture of axonemes revealed by cryoelectron tomography. *Science* 313: 944-948
864 Organization WH (2010) *WHO laboratory manual for the examination and processing of human*
865 *semen*. World Health Organization, Geneva
866 Padma P, Satouh Y, Wakabayashi K, Hozumi A, Ushimaru Y, Kamiya R, Inaba K (2003)
867 Identification of a novel leucine-rich repeat protein as a component of flagellar radial spoke in
868 the Ascidian Ciona intestinalis. *Mol Biol Cell* 14: 774-785
869 Pigino G, Bui KH, Maheshwari A, Lupetti P, Diener D, Ishikawa T (2011) Cryoelectron tomography
870 of radial spokes in cilia and flagella. *J Cell Biol* 195: 673-687
871 Ralston KS, Lerner AG, Diener DR, Hill KL (2006) Flagellar motility contributes to cytokinesis in
872 Trypanosoma brucei and is modulated by an evolutionarily conserved dynein regulatory system.
873 *Eukaryot Cell* 5: 696-711
874 Rao Q, Han L, Wang Y, Chai P, Kuo YW, Yang R, Hu F, Yang Y, Howard J, Zhang K (2021) Structures
875 of outer-arm dynein array on microtubule doublet reveal a motor coordination mechanism. *Nat*
876 *Struct Mol Biol* 28: 799-810
877 Rohou A, Grigorieff N (2015) CTFFIND4: Fast and accurate defocus estimation from electron
878 micrographs. *J Struct Biol* 192: 216-221
879 Satouh Y, Inaba K (2009) Proteomic characterization of sperm radial spokes identifies a novel
880 spoke protein with an ubiquitin domain. *FEBS Lett* 583: 2201-2207

881 Schindelin J, Arganda-Carreras I, Frise E, Kaynig V, Longair M, Pietzsch T, Preibisch S, Rueden C,
882 Saalfeld S, Schmid B *et al* (2012) Fiji: an open-source platform for biological-image analysis. *Nat*
883 *Methods* 9: 676-682
884 Shamseldin HE, Shaheen R, Ewida N, Bubshait DK, Alkuraya H, Almardawi E, Howaidi A, Sabr Y,
885 Abdalla EM, Alfaifi AY *et al* (2020) The morbid genome of ciliopathies: an update. *Genet Med* 22:
886 1051-1060
887 Shen Q, Martinez G, Liu H, Beurois J, Wu H, Amiri-Yekta A, Liang D, Kherraf ZE, Bidart M, Cazin C
888 *et al* (2021) Bi-allelic truncating variants in CFAP206 cause male infertility in human and mouse.
889 *Hum Genet* 140: 1367-1377
890 Sironen A, Shoemark A, Patel M, Loebinger MR, Mitchison HM (2020) Sperm defects in primary
891 ciliary dyskinesia and related causes of male infertility. *Cell Mol Life Sci* 77: 2029-2048
892 Slabbert M, du Plessis SS, Huyser C (2015) Large volume cryoprotectant-free vitrification: an
893 alternative to conventional cryopreservation for human spermatozoa. *Andrologia* 47: 594-599
894 Smith EF, Sale WS (1992) Regulation of dynein-driven microtubule sliding by the radial spokes in
895 flagella. *Science* 257: 1557-1559
896 Smith EF, Yang P (2004) The radial spokes and central apparatus: mechano-chemical transducers
897 that regulate flagellar motility. *Cell Motil Cytoskeleton* 57: 8-17
898 Soraggi S, Riera M, Meyts R-D, Schierup MH, Almstrup K (2021) Evaluating genetic causes of
899 azoospermia: What can we learn from a complex cellular structure and single-cell
900 transcriptomics of the human testis? *Human Genetics* 140: 183-201
901 Toure A, Martinez G, Kherraf ZE, Cazin C, Beurois J, Arnoult C, Ray PF, Coutton C (2021) The
902 genetic architecture of morphological abnormalities of the sperm tail. *Hum Genet* 140: 21-42
903 Urbanska P, Song K, Joachimiak E, Krzemien-Ojak L, Koprowski P, Hennessey T, Jerka-Dziadosz
904 M, Fabczak H, Gaertig J, Nicastro D *et al* (2015) The CSC proteins FAP61 and FAP251 build the
905 basal substructures of radial spoke 3 in cilia. *Mol Biol Cell* 26: 1463-1475
906 Van der Auwera GA, Carneiro MO, Hartl C, Poplin R, Del Angel G, Levy-Moonshine A, Jordan T,
907 Shakir K, Roazen D, Thibault J (2013) From FastQ data to high-confidence variant calls: the
908 genome analysis toolkit best practices pipeline. *Current protocols in bioinformatics* 43: 11.10.
909 11-11.10. 33
910 Viswanadha R, Sale WS, Porter ME (2017) Ciliary Motility: Regulation of Axonemal Dynein
911 Motors. *Cold Spring Harb Perspect Biol* 9
912 Witman GB, Plummer J, Sander G (1978) Chlamydomonas flagellar mutants lacking radial spokes
913 and central tubules. Structure, composition, and function of specific axonemal components. *J*
914 *Cell Biol* 76: 729-747
915 Yang H, Wang H, Jaenisch R (2014) Generating genetically modified mice using CRISPR/Cas-
916 mediated genome engineering. *Nature protocols* 9: 1956-1968
917 Yang P, Diener DR, Yang C, Kohno T, Pazour GJ, Dienes JM, Agrin NS, King SM, Sale WS, Kamiya R
918 *et al* (2006) Radial spoke proteins of Chlamydomonas flagella. *J Cell Sci* 119: 1165-1174
919 Yin W, Livraghi-Butrico A, Sears PR, Rogers TD, Burns KA, Grubb BR, Ostrowski LE (2019) Mice
920 with a Deletion of Rsph1 Exhibit a Low Level of Mucociliary Clearance and Develop a Primary
921 Ciliary Dyskinesia Phenotype. *Am J Respir Cell Mol Biol* 61: 312-321
922 Yoke H, Ueno H, Narita A, Sakai T, Horiuchi K, Shingyoji C, Hamada H, Shinohara K (2020) Rsph4a
923 is essential for the triplet radial spoke head assembly of the mouse motile cilia. *PLoS Genet* 16:
924 e1008664

925 Zhang X, Sun J, Lu Y, Zhang J, Shimada K, Noda T, Zhao S, Koyano T, Matsuyama M, Zhou S *et al*
926 (2021) LRRC23 is a conserved component of the radial spoke that is necessary for sperm motility
927 and male fertility in mice. *J Cell Sci* 134
928 Zhao Y, Pinskey J, Lin J, Yin W, Sears PR, Daniels LA, Zariwala MA, Knowles MR, Ostrowski LE,
929 Nicastro D (2021) Structural insights into the cause of human RSPH4A primary ciliary dyskinesia.
930 *Mol Biol Cell* 32: 1202-1209
931 Zheng S, Wolff G, Greenan G, Chen Z, Faas FGA, Barcena M, Koster AJ, Cheng Y, Agard DA (2022)
932 AreTomo: An integrated software package for automated marker-free, motion-corrected cryo-
933 electron tomographic alignment and reconstruction. *J Struct Biol X* 6: 100068
934 Zheng SQ, Palovcak E, Armache J-P, Cheng Y, Agard DA (2016) Anisotropic correction of beam-
935 induced motion for improved single-particle electron cryo-microscopy. *bioRxiv*: 061960
936 Zheng W, Li F, Ding Z, Liu H, Zhu L, Xu C, Li J, Gao Q, Wang Y, Fu Z *et al* (2021) Distinct
937 architecture and composition of mouse axonemal radial spoke head revealed by cryo-EM. *Proc*
938 *Natl Acad Sci U S A* 118
939 Zhu X, Liu Y, Yang P (2017) Radial Spokes-A Snapshot of the Motility Regulation, Assembly, and
940 Evolution of Cilia and Flagella. *Cold Spring Harb Perspect Biol* 9
941 Zivanov J, Otón J, Ke Z, von Kügelgen A, Pyle E, Qu K, Morado D, Castaño-Díez D, Zanetti G,
942 Bharat TAM *et al* (2022) A Bayesian approach to single-particle electron cryo-tomography in
943 RELION-4.0. *bioRxiv*: 2022.2002.2028.482229
944 Zou W, Lv Y, Liu ZI, Xia P, Li H, Jiao J (2020) Loss of Rsph9 causes neonatal hydrocephalus with
945 abnormal development of motile cilia in mice. *Sci Rep* 10: 12435

946

Figure Legends

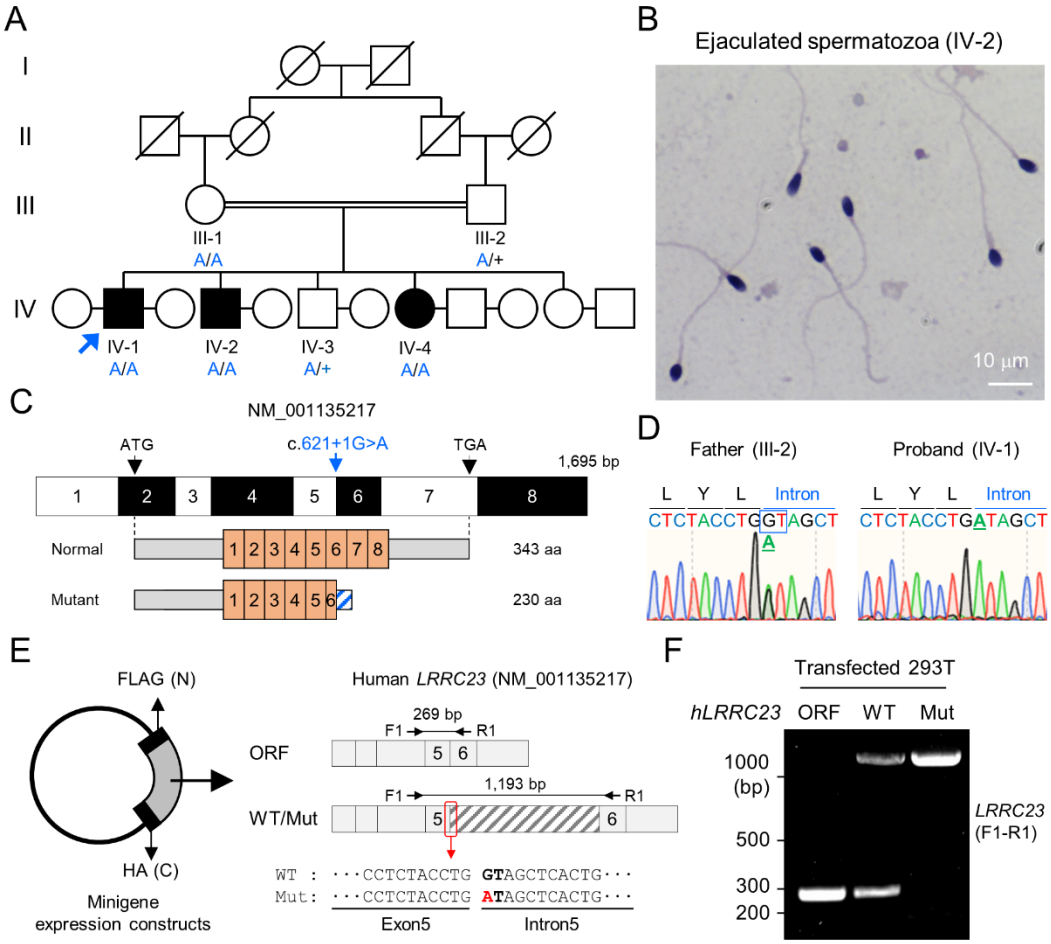

Figure 1. A bi-allelic splicing donor site variant in *LRRC23* was identified from asthenozoospermia patients.

A A consanguineous pedigree with two infertile males (IV-1 and IV-2). IV-1 was subjected for WES (arrow). Genotypes of the variant (blue) in all family members included in this study (III-1, III-2, IV-1, IV-2, IV-3, and IV-4) are confirmed by Sanger sequencing. +, wild-type allele. An infertile female sibling (IV-4) is marked in black circle.

B Papanicolaou-stained sperm from the infertile male (IV-2).

C Mapping of the LRRC23 variant. Mutation of G to A at the splicing donor site in the 5th intron is predicted to prevent *LRRC23* mRNA from splicing.

D Sequencing chromatograms presenting the *LRRC23* variant in the infertile male (IV-1) and his father (III-2). The variant is underlined and normal splicing donor site (GT) is boxed.

E, F Minigene assay for testing altered splicing of *LRRC23* by the variant. (E) Minigene constructs expressing *LRRC23* ORF containing the 5th intron (sashed) with wild-type (WT) or mutant (Mut, red) splicing donor site were generated. The constructs are tagged with FLAG and

HA at N- and C-termini, respectively. (F) RT-PCR of the 293T cells transfected with the minigene constructs reveals the 5th intron is not spliced out and retained by the variant. Intron-spanning primers, F1 and R1, are used. Repeated three times with biological replications.

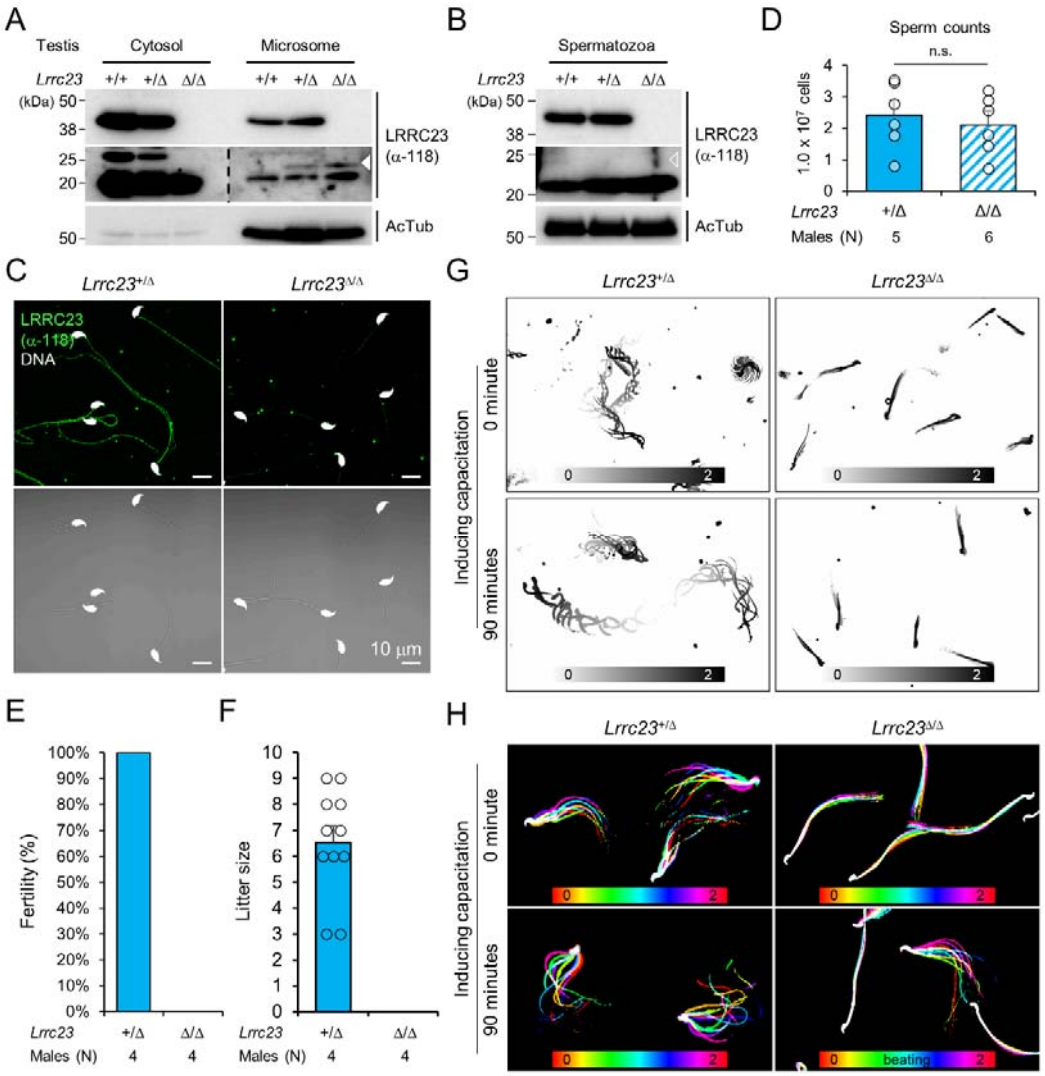

Figure 2. *Lrrc23* mutant mice mimicking human splice variant phenocopy male infertility and reduced sperm motility.

A, B Immunoblotting of LRRC23 in testis (A) and epididymal sperm (B) from mutant male mice. Truncated LRRC23 (arrowheads) is detected from testis microsome fraction (filled), but not in mature sperm (empty), of heterozygous (+/Δ) and homozygous (Δ/Δ) males. Acetylated tubulin (AcTub) is a loading control. Experiments were performed with three biological replications.

C Confocal images of immunostained LRRC23 in *Lrrc23*$^{+/\Delta}$ and *Lrrc23*$^{\Delta/\Delta}$ epididymal sperm Experiments were repeated with three biological replications.

D Epididymal sperm counts. n.s., not significant.

E Pregnancy rate of *Lrrc23*$^{+/\Delta}$ and *Lrrc23*$^{\Delta/\Delta}$ males.

F Number of litters from fertile females mated with *Lrrc23*$^{+/\Delta}$ and *Lrrc23*$^{\Delta/\Delta}$ males.

G Swimming trajectory of *Lrrc23*$^{+/\Delta}$ and *Lrrc23*$^{\Delta/\Delta}$ sperm in viscous media (0.3% methylcellulose). Swimming trajectory for 2 seconds is overlaid. Experiments were performed

with three biological replications. See Movie EV1.

H Flagellar waveforms of *Lrrc23*$^{+/\Delta}$ and *Lrrc23*$^{\Delta/\Delta}$ sperm before (0 minute) and after (90 minutes) inducing capacitation. Flagellar movements for two beat cycles are overlaid and color coded in time. Experiments were performed with three biological replications. See Movie EV2.

Data information: In (A-C), samples from WT were used for positive or negative control of normal or truncated LRRC23. In (D, F), circles indicate sperm counts from individual males (D) and pup numbers from each litter (F), and data represented as mean ± SEM (D, Mann-whiteny U test; F, Student's t-test). n.s., non-significant.

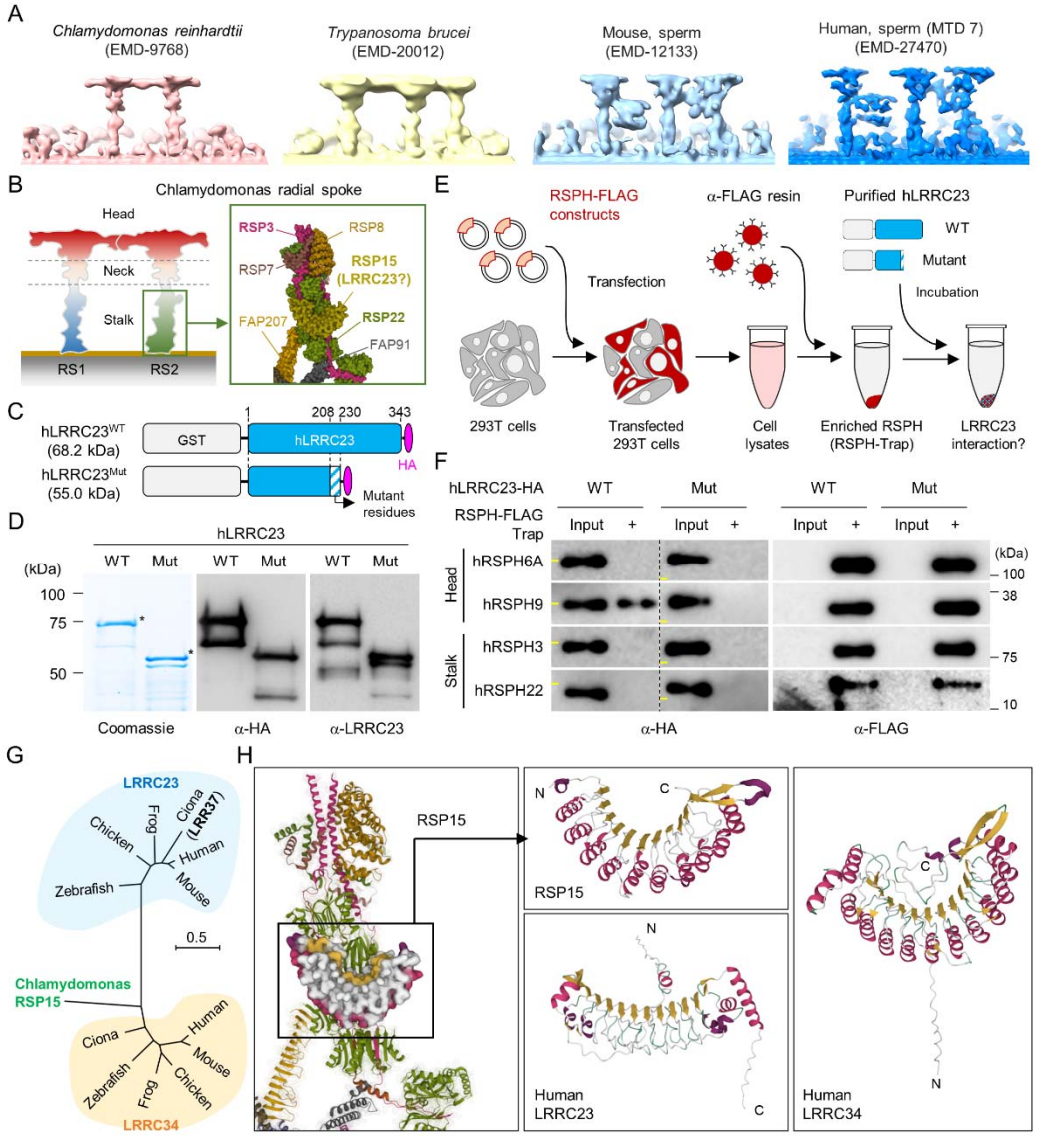

Figure 3. C-terminal truncation of human LRRC23 by the splicing site mutation prevents its interaction with radial spoke (RS) head.

A Sub-tomogram averaging images of RSs from *Chlamydomonas reinhardtii* (*red*), *Trypanosoma brucei* (yellow), mouse sperm (sky blue), and human sperm (blue). RSs at 7th microtubule doublet (MTD) are shown for human sperm. Original data from Electron Microscopy Data Bank was rendered.

B Structure of RS in *C. reinhardtii*. A schematic cartoon shows the RS1 and 2. The structure of RS2 stalk is shown in inset (PDB Id: 7JRJ).

C, D Purification of normal (hLRRC23^{WT}) and the mutant human LRRC23 (hLRRC23^{Mut}) by the splicing site mutation (c.621+1G>A) in this study. (C) Diagrams for the purified recombinant normal and mutant proteins tagged with tagged with GST and HA at N- and C-termini, respectively. (D) Purified proteins by Coomassie blue staining (*left*) and immunoblotting with α-HA (*middle*) and a-LRRC23 (*right*). Proteins matched to the predicted size were marked with

asterisks.

E A cartoon of the RSPH-trap approach to test LRRC23 interaction with RS proteins. Individual human RS proteins tagged with FLAG (RSPH-FLAG) are expressed in 293T cells and enriched by α-FLAG resin from cell lysates. The recombinant RSPH proteins were incubated with the purified $hLRRC23^{WT}$ or $hLRRC23^{Mut}$ and subjected to immunoblotting.

F Interaction of hLRRC23 to a RS head component, RSPH9. The purified hLRRC23 were incubated with the RSPH-Trap (RS head, RSPH6A and RSPH9; stalk, RSPH3 and RSPH22) and subjected to immunoblotting. 5% amount of the hLRRC23s used for the trap assay were loaded as inputs. Yellow lines in individual α-HA blot images indicate marker information (75 kDa, *left*; 50 kDa, *right*). Experiments were repeated four times. Purified GST was used for negative control (Fig EV4B). Experiments were repeated three times with biological replications.

G A phylogenetic tree constructed by Maximum-likelihood analysis of the protein sequences of the *C. reinhardtii* RSP15 and the orthologs of LRRC23 and LRRC34. LRR37, the first LRRC23 ortholog identified in *Ciona intestinalis* is marked in bold.

H Comparison of the reported RSP15 from *C. reinhardtii* and the predicted structure of LRRC23 and LRRC34 from human. Atomic structure of the *C. reinhardtii* RS2 containing RSP15 are represented by ribbon (RS2) and surface (RSP15) diagram (*left*, PDB Id: 7JU4). Ribbon diagrams of *C. reinhardtii* RSP15 and AlphaFold-predicted human LRRC23 (*middle*) and LRRC34 (*right*) are shown for structural comparison. Secondary structures are color-coded. Different from *C. reinhardtii* RSP15 and LRRC34, LRRC23 does not display repeated α-helix (magenta) between β-sheets (gold).

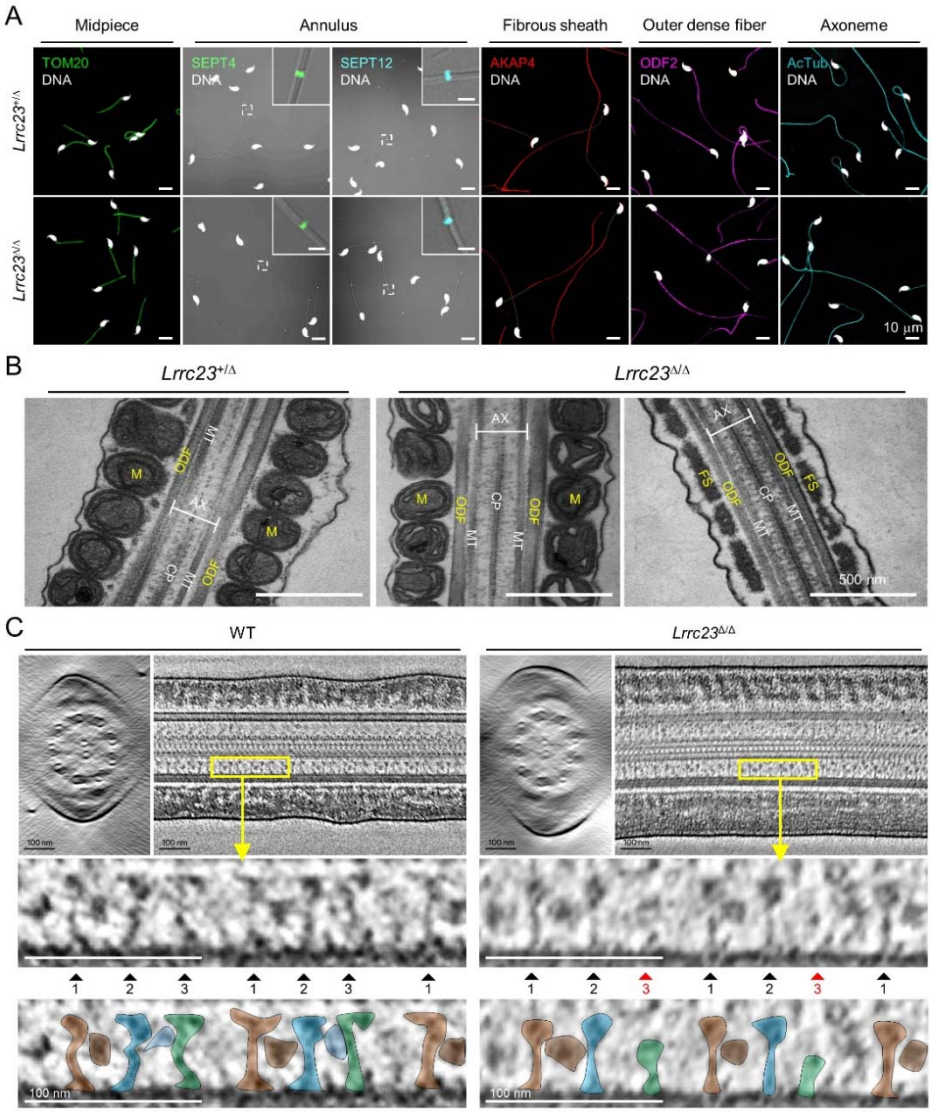

Figure 4. LRRC23 mutation disrupts the third radial spoke (RS) in sperm flagellum.

A Immunostaining of flagellar proteins in different compartments. Shown are midpiece (TOM20), annulus (SEPT4 and SEPT12), fibrous sheath (AKAP4), outer dense fiber (ODF2), and axoneme (acetylated tubulin, AcTub) in *Lrrc23*$^{+/\Delta}$ (*top*) and *Lrrc23*$^{\Delta/\Delta}$ (*bottom*) sperm. Magnified insets are represented for annulus proteins (scale bars in insets = 2μm). Fluorescence and corresponding DIC images are merged. Sperm heads were counter stained with Hoechst. *Lrrc23*$^{+/\Delta}$ sperm were used for positive control. Experiments were performed with three biological replications.

B Transmission electron microscopy images of *Lrrc23*$^{+/\Delta}$ (*left*) and *Lrrc23*$^{\Delta/\Delta}$ (*right*) sperm. Shown are longitudinal section of sperm flagella. M, mitochondria; ODF, outer dense fiber; AX, axoneme; CP, central pair; MT, microtubule; FS, fibrous sheath. *Lrrc23*$^{+/\Delta}$ sperm were used for positive control.

C Cryo-electron tomography (cryo-ET) of WT and *Lrrc23*$^{\Delta/\Delta}$ sperm flagella. Shown are representative tomographic slices from WT (*left*) and *Lrrc23*$^{\Delta/\Delta}$ sperm (*right*). The 9+2 axonemal

structure are shown in both WT and *Lrrc23*$^{\Delta/\Delta}$ in cross-sectional view (*left*). Axonemal structures are shown with proximal side of the flagellum on the left in longitudinal view (*right*; see Movie EV3). Magnified insets (*bottom*) reveal that RS1, 2, and 3 are shown in WT sperm (*left*, filled arrowheads) but RS3, especially head part, is not clearly visible (*right*, red arrowheads) in *Lrrc23*$^{\Delta/\Delta}$ sperm. RS1, 2, and 3 are distinguished by the interval between each set of RS1, 2, and 3, and the electron dense area corresponding to the barrel (RS1) and bridge (RS2-3) structures. WT sperm were used for positive control.

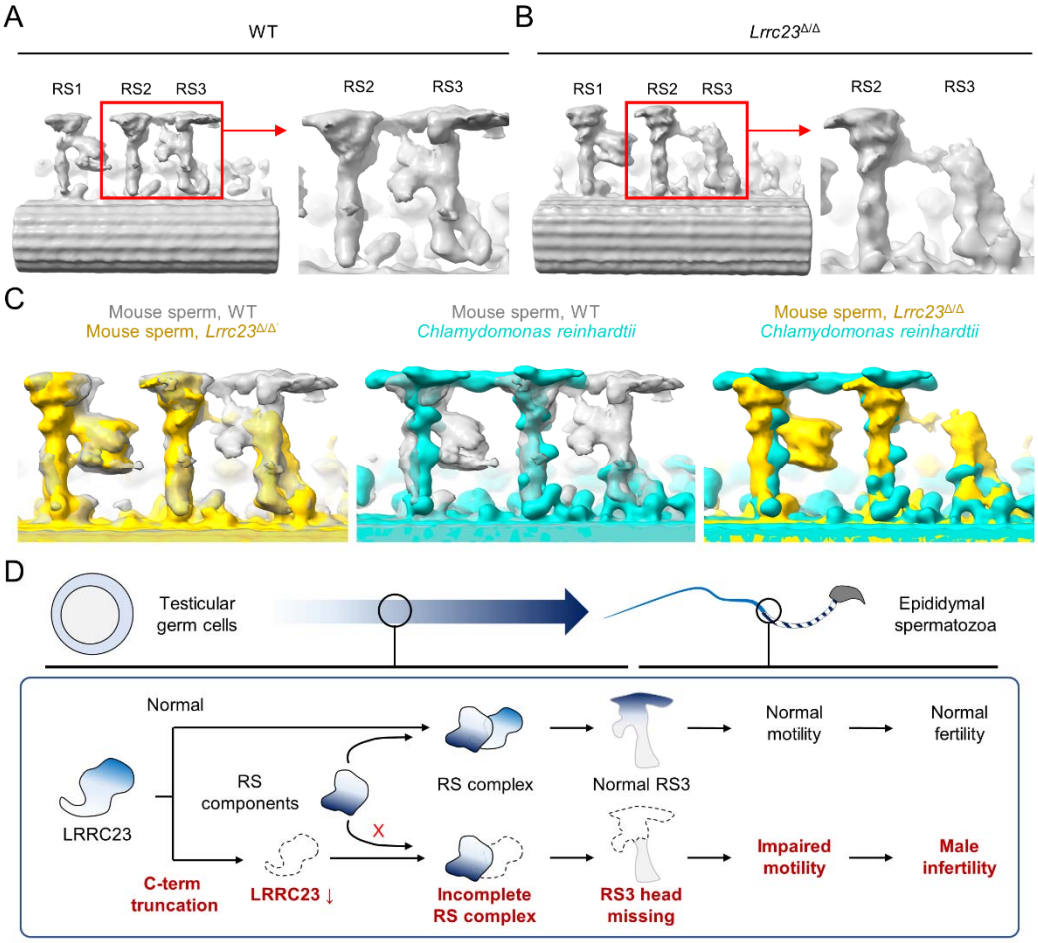

Figure 5. Head of the third radial spoke is absent in *Lrrc23*$^{\Delta/\Delta}$ sperm flagella.

A, B Sub-tomogram averaging (STA) to analyze structural defects at radial spoke (RS) of WT (A) and *Lrrc23*$^{\Delta/\Delta}$ sperm (B). Shown are STA images resulted from 96-nm doublet repeats from WT and *Lrrc23*$^{\Delta/\Delta}$ sperm. RS2 and 3 are magnified and density to represent RS3 head and the bridge between RS2 and RS3 (red circle) is missed in *Lrrc23*$^{\Delta/\Delta}$ sperm specifically.

C Overwrapped STA images from 96 nm-doublet repeats from WT (gray) and *Lrrc23*$^{\Delta/\Delta}$ (gold) sperm, and *Chlamydomonas reinhardtii* (cyan).

D A proposed model of impaired sperm motility and male infertility by the LRRC23 loss of function.

Expanded View Figure Legends

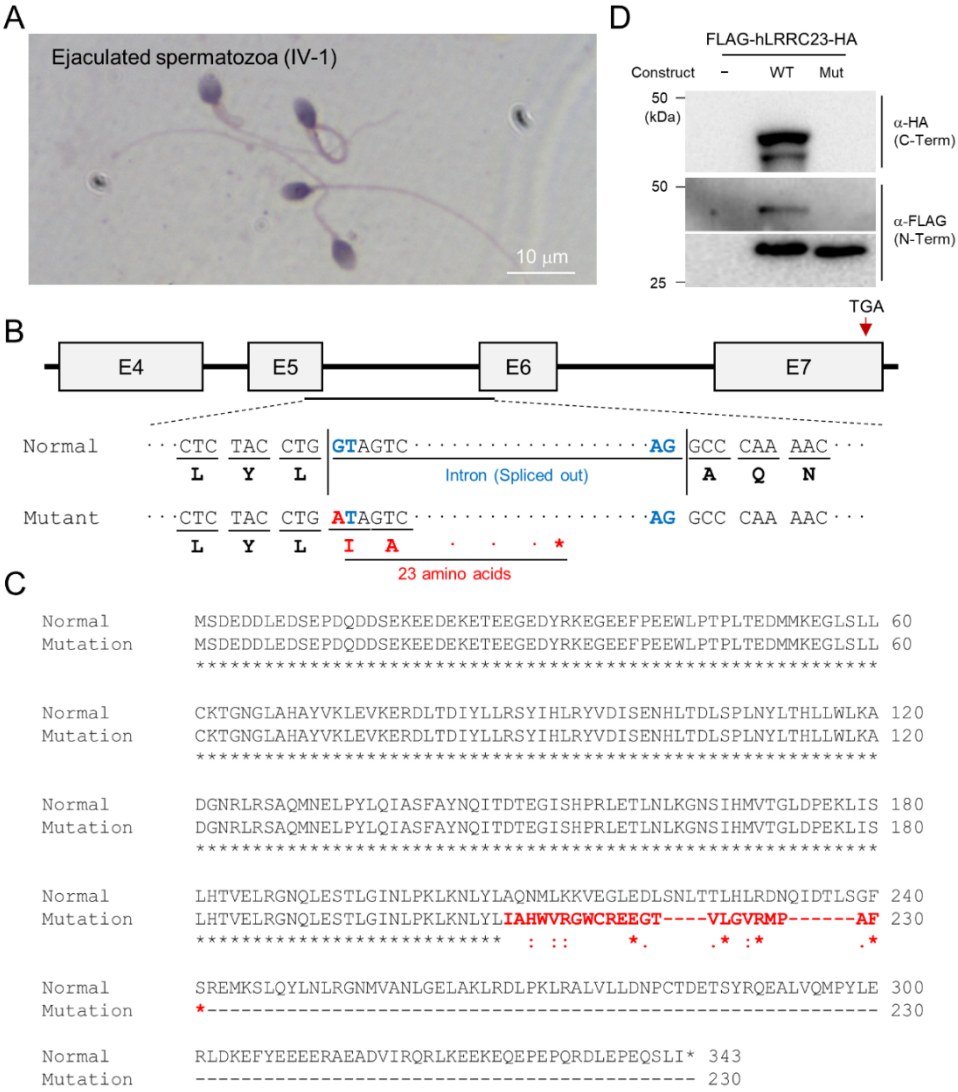

Figure EV1. A *LRRC23* splicing site variant identified from infertile male patients.

A Papanicolaou-stained sperm from the infertile male member, IV-2.

B The splicing site variant in the 5th intron of *LRRC23* gene. The variant is predicted to cause early termination of the protein translation.

C Sequence alignment of the normal and predicted mutant LRRC23 by the splicing site mutation. Non-native amino acid sequences encoded by the mutant allele are colored in red.

D Immunoblot analysis of 293T cells transfected with the human *LRRC23* minigene constructs containing the 5th intron. The construct carrying the intron with the identified variant generate only a truncated LRRC23. Non-transfected cells (NTC) are used for a negative control. Three biological replications.

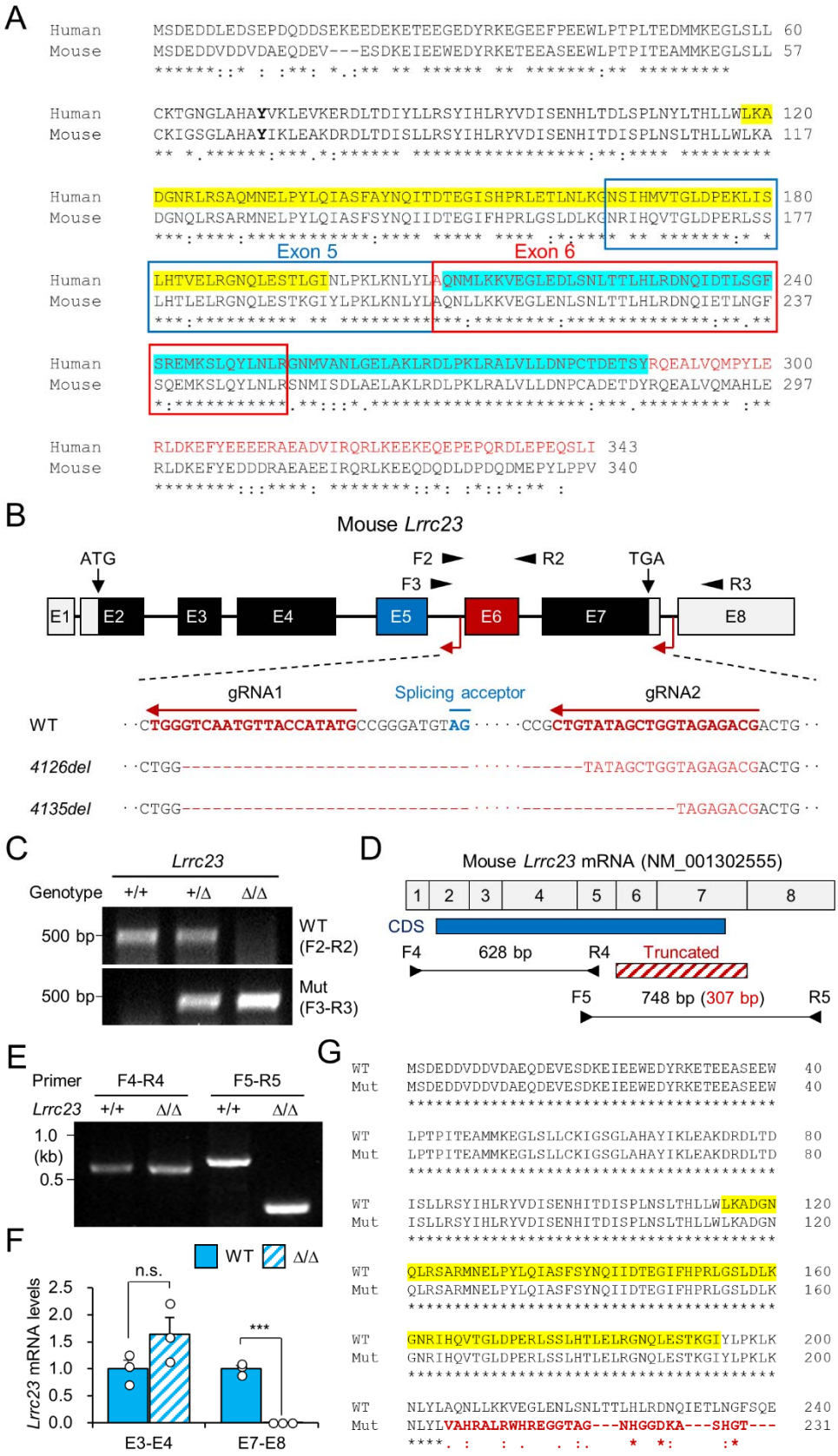
A
Human MSDEDDLEDSEPDQDDSEKEEDEKETEEGEDYRKEGEEFPEEWLPTPLTEDMMKEGLSLL 60
Mouse MSDEDDVDDVDAEQDEV---ESDKEIEEWEDYRKETEEASEEWLPTPITEAMMKEGLSLL 57
Human CKTGNGLAHAYVKLEVKERDLTDIYLLRSYIHLRYVDISENHLTDLSPLNYLTHLLWLKA 120
Mouse CKIGSGLAHAYIKLEAKDRDLTDISLLRSYIHLRYVDISENHITDISPLNSLTHLLWLKA 117
Human DGNRLRSAQMNELPYLQIASFAYNQITDTEGISHPRLETLNLKGNSIHMVTGLDPEKLIS 180
Mouse DGNQLRSARMNELPYLQIASFSYNQIIDTEGIFHPRLGSLDLKGNRIHQVTGLDPERLSS 177
Exon 5
Exon 6
Human LHTVELRGNQLESTLGINLPKLKNLYLAQNMLKKVEGLEDLSNLTTLHLRDNQIDTLSGF 240
Mouse LHTLELRGNQLESTKGIYLPKLKNLYLAQNLLKKVEGLENLSNLTTLHLRDNQIETLNGF 237
Human SREMKSLQYLNLRGNMVANLGELAKLRDLPKLRALVLLDNPCTDETSYRQEALVQMPYLE 300
Mouse SQEMKSLQYLNLRSNMISDLAELAKLRDLPKLRALVLLDNPCADETDYRQEALVQMAHLE 297
Human RLDKEFYEEEERAEADVIRQRLKEEKEQEPEPQRDLEPEQSLI 343
Mouse RLDKEFYEDDDRAEAEEIRQRLKEEQDQDLDPDQDMEPYLPPV 340
B
Mouse Lrrc23
ATG
F2
R2
TGA
F3
R3
E1
E2
E3
E4
E5
E6
E7
E8
gRNA1
Splicing acceptor
gRNA2
WT ··CTGGGTCAATGTTACCATATGCCGGGATGTAG·····CCGCTGTATAGCTGGTAGAGACGACTG··
4126del ··CTGG----------·····-------TATAGCTGGTAGAGACGACTG··
4135del ··CTGG----------·····----------TAGAGACGACTG··
C
Lrrc23
Genotype +/+ +/Δ Δ/Δ
500 bp
WT (F2-R2)
500 bp
Mut (F3-R3)
D
Mouse Lrrc23 mRNA (NM_001302555)
1 2 3 4 5 6 7 8
CDS
F4
628 bp
R4
Truncated
F5
748 bp (307 bp)
R5
E
Primer F4-R4 F5-R5
Lrrc23 +/+ Δ/Δ +/+ Δ/Δ
1.0 (kb) 0.5
F
WT Δ/Δ
n.s.
***
Lrrc23 mRNA levels
2.5 2.0 1.5 1.0 0.5 0.0
E3-E4
E7-E8
G
WT MSDEDDVDDVDAEQDEVESDKEIEEWEDYRKETEEASEEW 40
Mut MSDEDDVDDVDAEQDEVESDKEIEEWEDYRKETEEASEEW 40
WT LPTPITEAMMKEGLSLLCKIGSGLAHAYIKLEAKDRDLTD 80
Mut LPTPITEAMMKEGLSLLCKIGSGLAHAYIKLEAKDRDLTD 80
WT ISLLRSYIHLRYVDISENHITDISPLNSLTHLLWLKADGN 120
Mut ISLLRSYIHLRYVDISENHITDISPLNSLTHLLWLKADGN 120
WT QLRSARMNELPYLQIASFSYNQIIDTEGIFHPRLGSLDLK 160
Mut QLRSARMNELPYLQIASFSYNQIIDTEGIFHPRLGSLDLK 160
WT GNRIHQVTGLDPERLSSLHTLELRGNQLESTKGIYLPKLK 200
Mut GNRIHQVTGLDPERLSSLHTLELRGNQLESTKGIYLPKLK 200
WT NLYLAQNLLKKVEGLENLSNLTTLHLRDNQIETLNGFSQE 240
Mut NLYLVAHRALRWHREGGTAG---NHGGDKA---SHGT--- 231

Figure EV2. **Generation of LRRC23 mutant mouse models.**

A A pair-wise alignment of human and mouse LRRC23 protein sequences. Deleted amino acids by the splice site mutation (encoded by exon 6 and 7) are written in red. Epitopes for the LRRC23 antibodies against N- (118-197, yellow) and C-terminus (209-288, cyan) are highlighted.

B Generation of LRRC23 mutant mouse models by CRISPR/Cas9 genome editing. Two guide RNAs targeting 5th and 7th intron were used to generate mouse models expressing LRRC23 lacking C-terminus like the predicted human mutant LRRC23. Two mutant alleles with 4126 (*Lrrc23-4126del*) or 4135 bp (*Lrrc23-4135del*) deletion were established.

C Genotyping of the generated mouse models. Primer locations are marked in panel (B). *Lrrc23-4126del*$^{\Delta/\Delta}$ and *Lrrc23-4135del* $^{\Delta/\Delta}$ mice show the identical phenotypes. *Lrrc23-4126*$^{\Delta/\Delta}$ mice were used as *Lrrc23*$^{\Delta/\Delta}$ mice in this study unless indicated.

D-F *Lrrc23* mRNA expression in testis from *Lrrc23* mutant males. (D) Shown is a diagram of exon composition of mouse *Lrrc23* mRNA (NM_001302555). Protein coding region (CDS), truncated exons in the mutant allele, and primers for RT-PCR are marked. A primer pair spanning truncated region (F5-R5) amplifies 748 bp and 307 bp PCR product from WT and the mutant alleles, respectively. (E) Endpoint and (F) real-time RT-PCR analyses of *Lrrc23* mRNA expression in *Lrrc23*$^{\Delta/\Delta}$ testis. Primers amplifying exon 3 and4 (E3-E4) and exon 7 and 8 (E7-E8) were used for real-time RT-PCR. Circles indicate relative levels from individual animals. N=3 for real-time PCR. Statistical analysis was performed by Student's t-test. n.s., not significant; $p^{***}<0.001$.

G A pair-wise sequence alignment of WT and the predicted mutant LRRC23 proteins generated from the truncated allele. Non-native sequences from the truncated *Lrrc23* mRNA are colored in red.

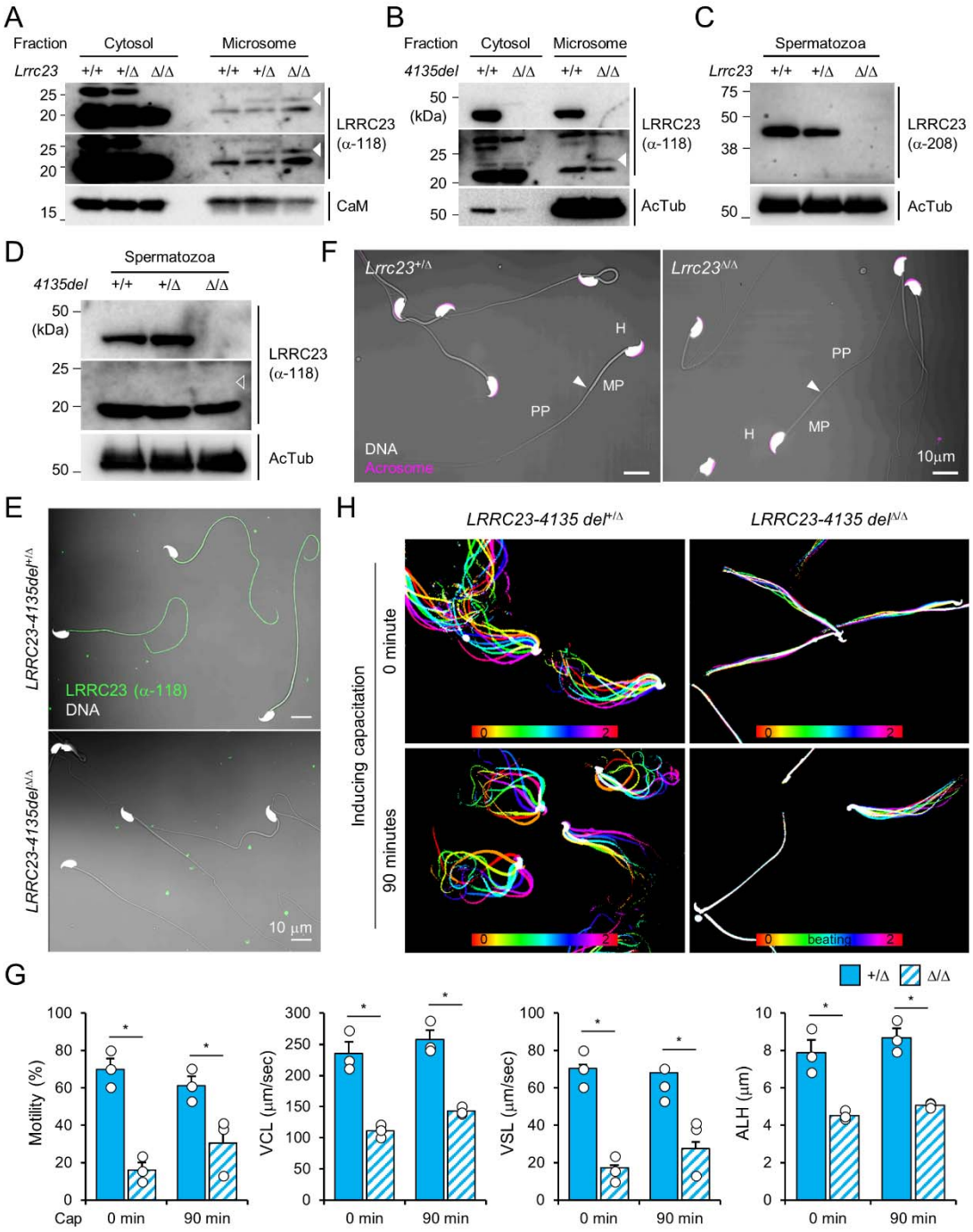

Figure EV3. Characterization of the *Lrrc23* loss of function male mice.

A-D Protein expression of LRRC23 in wild type (WT) and *Lrrc23* mutant males. (A) Original images of truncated LRRC23 immunoblotting in testis shown in Fig. 2A. Short (*top*) and long (*middle*) exposure images are shown. Calmodulin (CaM) is a loading control. (B) Immunobloting of LRRC23 in testis from *Lrrc23-4135del* mutant males. (C) LRRC23 immunoblotting in epididymal sperm from WT, *Lrrc23*$^{+/\Delta}$, and *Lrrc23*$^{\Delta/\Delta}$ males. (D) Immunoblotting of LRRC23 in WT

and *Lrrc23-4135del*$^{\Delta/\Delta}$ sperm. Truncated LRRC23 (arrowheads) is detected from testis (filled, A and B), but not from epididymal sperm (empty, D) of *Lrrc23* mutant males. Acetylated tubulin (AcTub) is a loading control. Samples from WT males were used for either positive or negative controls of normal and truncated LRRC23, respectively (A, B, C, and D).

E Confocal images of immunostained LRRC23 in *Lrrc23-4135del*$^{+/\Delta}$ and *Lrrc23-4135del*$^{\Delta/\Delta}$ sperm.

F Confocal images of epididymal sperm from *Lrrc23*$^{+/\Delta}$ and *Lrrc23*$^{\Delta/\Delta}$ males. Acrosome is stained with wheat-germ agglutinin. Arrowheads indicate the annulus.

G Computer assisted sperm analysis (CASA) to measure motility parameters of *Lrrc23*$^{+/\Delta}$ and *Lrrc23*$^{\Delta/\Delta}$ sperm. Sperm motility parameters were measured before (0 min) and after (90 min) inducing capacitation. VCL, curvilinear velocity; VSL, straight line velocity; ALH, amplitude of lateral head. Mann-Whitney U test was used for statistical comparison. *$p \leq 0.05$. N=3. Circles indicate values from individual animals. Data is represented as mean ± SEM.

H Flagellar movement of the *Lrrc23-4135del*$^{+/\Delta}$ (*left*) and *Lrrc23-4135del*$^{\Delta/\Delta}$ (*right*). Shown are overlays of sperm tail movement over two beat cycles before (0 min, *top*) and after (90 min, *bottom*) inducing capacitation.

Used are LRRC23 antibodies recognizing N- (α-118) or C- (α-208) terminal region (A, B, C, D, and E). Hoechst is used for counterstaining DNA and fluorescence and DIC images are merged (E and F). All experiments were carried out with over three biological replications.

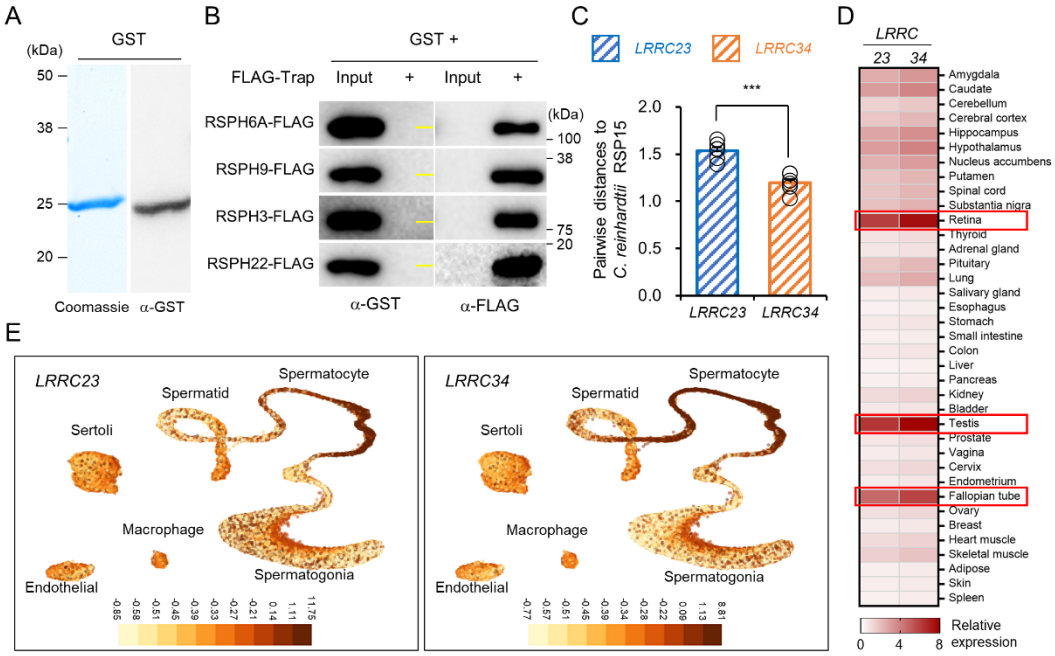

Figure EV4. A predicted RSP15 ortholog, *LRRC34*, in metazoan species.

A Purified recombinant GST confirmed by Coomassie blue staining (*left*) and immunoblotting (*right*).

B Interaction test of GST to human radial spoke proteins (RSPH) by trap-assay as a negative control. Yellow lines in α-GST blot images indicate molecular weight (25 kDa).

C Comparison of the pairwise distances of *Chlamydomonas reinhardtii* RSP15 to the LRRC23 or LRRC34 orthologs. Protein sequences of *C. reinhardtii* RSP15 and the metazoan LRRC23 and LRRC34 orthologs were aligned and pairwise distances were calculated. Protein sequences of the *C. reinhardtii* RSP15 are closer to LRRC34 orthologs evolutionarily than LRRC23 orthologs in metazoan. Statistical analysis was performed by Student's t-test. ***$p<0.001$, Data is represented by mean ± SEM.

D A heatmap to represent human tissue mRNA expression of *LRRC23* and *LRRC34*. Relative mRNA expression levels were calculated by normalizing tissue nTPM values with the median values. Three tissues with the highest *LRRC23* and *LRRC34* mRNA levels are highlighted. RNA GTEx tissue gene data from The Human Cell Atlas was used.

E *LRRC23* (*left*) and *LRRC34* (*right*) mRNA expression in human testicular cells. mRNA levels in individual cells are represented by UMAP plots downloaded from UCSC cell browser.

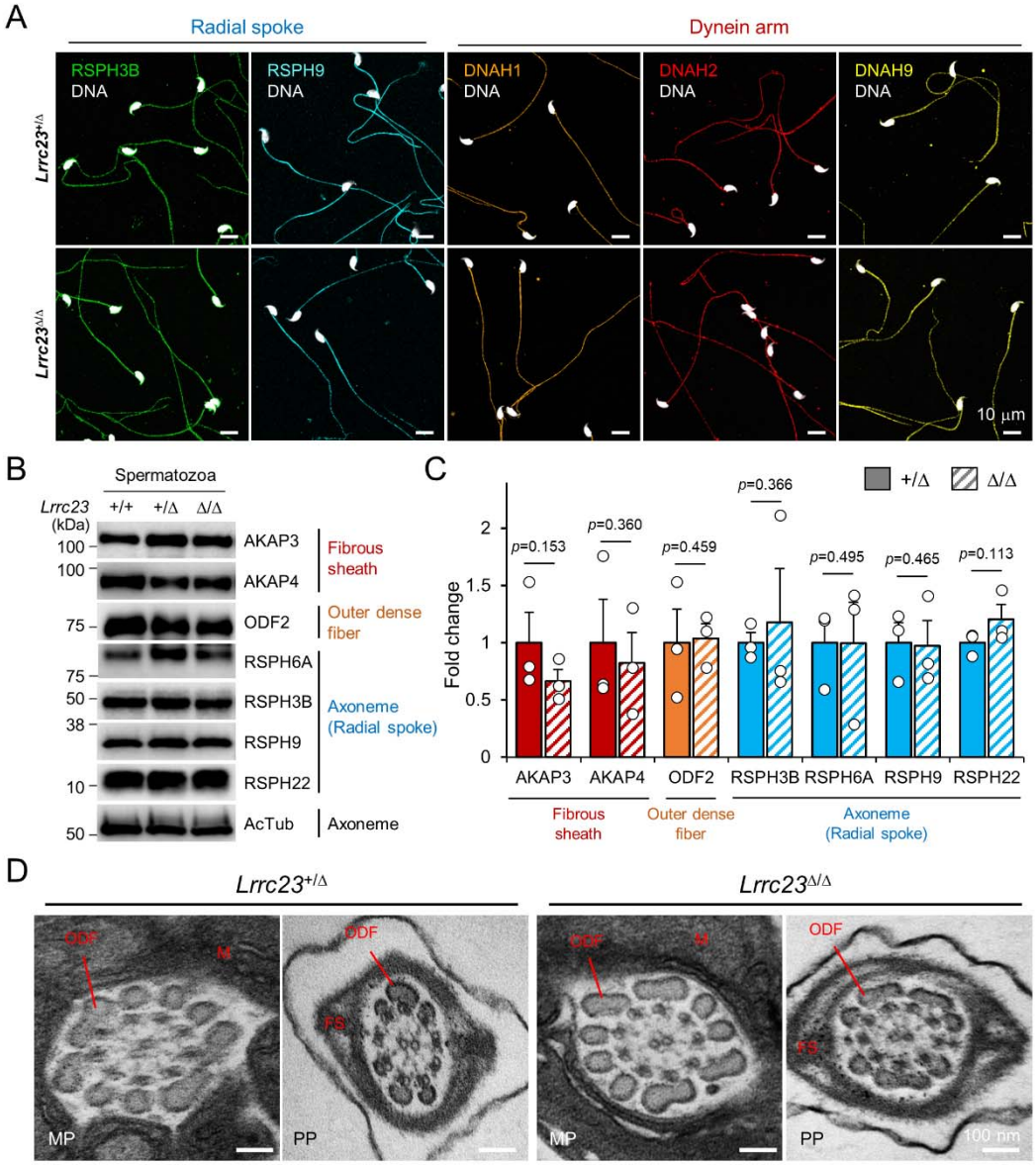

Figure EV5. Flagellar compartmentalization in *Lrrc23*-mutant sperm.

A Distribution of the axonemal components in *Lrrc23*$^{\Delta/\Delta}$ sperm. Immunostained radial spoke (RSPH3B and RSPH9) and dynein arm (DNAH1, DNAH2, and DNAH9) in *Lrrc23*$^{+/\Delta}$ and *Lrrc23*$^{\Delta/\Delta}$ sperm are shown by confocal images. Hoechst is used for counterstaining the sperm head. Experiment was performed with three biological replications.

B, C Unaffected protein levels of the representative components of fibrous sheath, outer dense fiber, and axoneme in *Lrrc23*$^{\Delta/\Delta}$ sperm. (B) Immunoblotting of the flagellar components in cauda sperm. Acetylated tubulin (AcTub) is a loading control. (C) Fold-changes of the flagellar components levels in *Lrrc23*$^{+/\Delta}$ (filled) and *Lrrc23*$^{\Delta/\Delta}$ (sash) sperm. Relative protein levels were quantified by measuring the band intensity and normalized by the AcTub intensity. The average level of each protein in *Lrrc23*$^{+/\Delta}$ sperm is set to 1-fold. Circles represents fold changes of each sperm protein from individual males. Data represented as mean ± SEM. Statistical analysis was

performed by Student's t-test. N=3.

D Transmission electron microscopy (TEM) images of epididymal sperm from *Lrrc23*$^{+/\Delta}$ and *Lrrc23*$^{\Delta/\Delta}$ males. Shown are representative cross section TEM images of *Lrrc23*$^{+/\Delta}$ (*left*) and *Lrrc23*$^{\Delta/\Delta}$ (*right*) sperm. No obvious structural defects at the midpiece (MP) and principal piece (PP) were observed from and *Lrrc23*$^{\Delta/\Delta}$ sperm. M, mitochondria; FS, fibrous sheath; ODF, outer dense fiber; AX, axoneme.

WT and/or *Lrrc23*$^{+/\Delta}$ sperm were used for positive control (A, B, C and D).

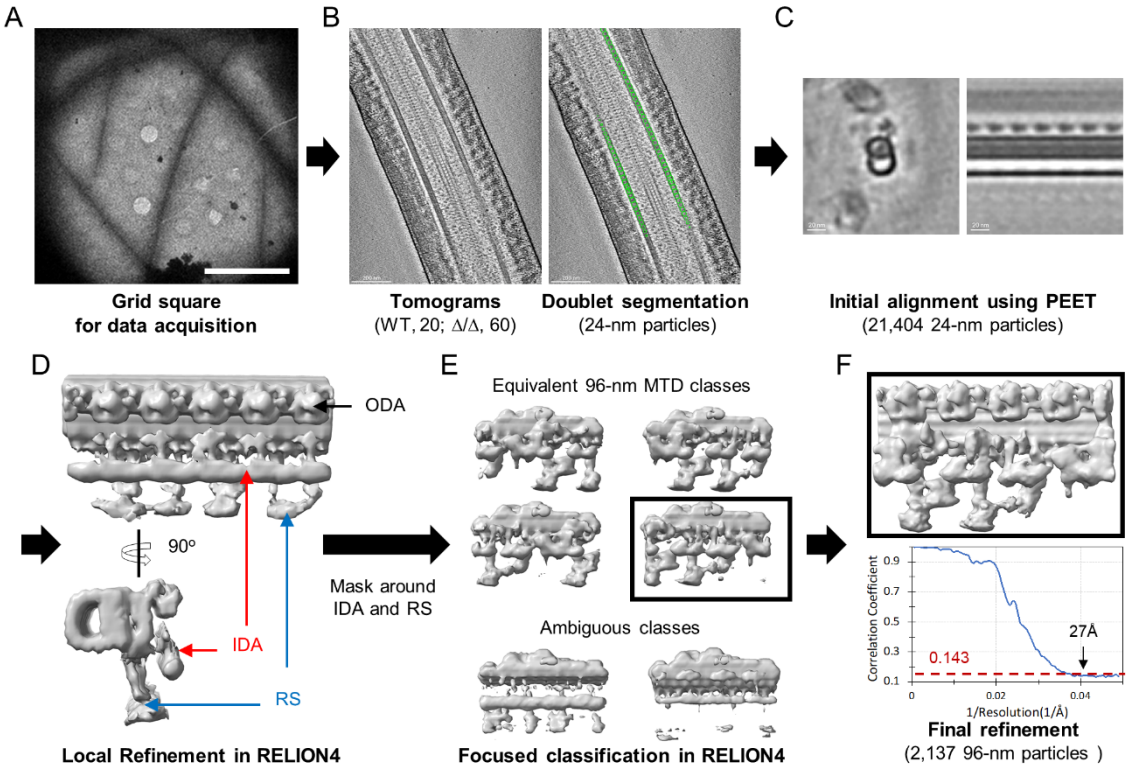

Figure EV6. Workflow of cryo-electron tomography (cryo-ET) and sub-tomogram averaging (STA) processing of 96-nm microtubule doublet repeat from mouse sperm.

A An example of low magnification map of *Lrrc23*$^{\Delta/\Delta}$ mouse sperm on grid square. Scale bar, 10 µm.

B An example tomographic slice obtained from sperm on the grid and segmented particles with 24 nm interval (green circles, *right*).

C Initial alignment using PEET. Cross-sectional (*left*) and longitudinal (*right*) views are shown. D Local refinement of 24-nm particles in RELION4 after coordination and Euler angles transform. Density for outer dynein arm (ODA, black arrow) are visualized. Densities to represent inner dynein arm (IDA, red arrows) and radial spoke (RS, blue arrows) were averaged due to symmetry mismatch.

E A soft-edge mask around IDA and RS. 96-nm repeat of microtubule doublet (MTD) classes with different translational symmetries (*top*) were obtained using focused classification in RELION4. The ambiguous classes (*bottom*) were discarded.

F Final local refinement using one 96-nm repeat class. The gold-standard Fourier Shell Correlation (FSC) curve is shown at bottom.

Expanded View Tables and Movies

Table EV1. Clinical diagnosis of the infertile patients

Table EV2. Variant Detail in the infertility Family

Table EV3. Summarized imaging acquisition parameters and 3D refinement statistics

Movie EV1. *Lrrc23*$^{+/\Delta}$ and *Lrrc23*$^{\Delta/\Delta}$ sperm swimming freely in a viscous environment. Free-swimming *Lrrc23*$^{+/\Delta}$ and *Lrrc23*$^{\Delta/\Delta}$ sperm in the viscous condition containing 0.3% methylcellulose were recorded for 2 seconds before and after inducing capacitation for 90 minutes. Individual videos are played at 50 fps (1/2 speed).

Movie EV2. Flagellar waveform of *Lrrc23*$^{+/\Delta}$ and *Lrrc23*$^{\Delta/\Delta}$ sperm before and after inducing capacitation. Tail movements of head-tethered sperm from *Lrrc23*$^{+/\Delta}$ and *Lrrc23*$^{\Delta/\Delta}$ males are recorded for 2 seconds before and after incubation under capacitating conditions for 90 minutes. Each video is played at 100 fps (1/2 speed).

Movie EV3. Tilted series of cryo-electron tomogram slices from WT (*left*) and *Lrrc23*$^{\Delta/\Delta}$ (*right*) spermatozoa. Tomogram images were acquired of WT and *Lrrc23*$^{\Delta/\Delta}$ sperm were acquired on the grid and image slices were rendered to show the axonemal structure in a tilt series.